

Thermophysical characteristics and application of metallic–oxide based mono and hybrid nanocomposite phase change materials (NCPCMs) for thermal management systems.

Adeel Arshad^a, Mark Jabbal^a, Yuying Yan^{a,b,*}

^a*Fluids & Thermal Engineering (FLUTE) Research Group, Faculty of Engineering, University of Nottingham, Nottingham, NG7 2RD, UK*

^b*Research Centre for Fluids and Thermal Engineering, University of Nottingham Ningbo China, Ningbo 315100, China*

Abstract

This experimental study covers the chemical, physical, thermal characterization and application of novel nanocomposite phase change materials (NCPCMs) dispersed by TiO₂, Al₂O₃, and CuO nanoparticles. A commercial-grade of paraffin, namely RT–35HC, was considered as a phase change material (PCM). The mono and hybrid NCPCMs were synthesized at a constant weight concentration of 1.0 wt.%. In the first phase, various characterization techniques were used to explore the thermophysical properties and chemical interaction of mono and hybrid NCPCMs. In the second phase, the thermal cooling performance was investigated by filling the prepared NCPCMs in a heat sink at various input power levels. The results showed the uniform dispersion of TiO₂, Al₂O₃, and CuO nanoparticles onto the surface of both mono and hybrid NCPCMs without altering the chemical structure of RT–35HC. The optimum latent–heat of fusion and highest thermal conductivity of 228.46 J/g and 0.328 W/m.K were obtained, respectively, of Al₂O₃+CuO dispersed hybrid NCPCM compared to pure RT–35HC. In comparison of RT–35HC, the increasing trend in specific heat capacity was observed of NCPCMs and 36.47% enhancement was obtained for hybrid NCPCM in solid–phase. The reduction in heat sink base temperature was achieved of 3.67%, 6.13%, 13.95% and 8.23% for NCPCM_{TiO₂}, NCPCM_{Al₂O₃}, NCPCM_{CuO} and NCPCM_{Al₂O₃+CuO}, respectively, compared to RT-35HC. Further, no phase segregation, less subcooling, smaller phase transition temperature, higher chemical and thermal stability were observed with hybrid NCPCMs which can be used potentially for thermal management of electronic devices, Li-ion batteries and photovoltaic (PV) modules systems.

Keywords: Phase change material, TiO₂, Al₂O₃, CuO, Nanocomposite phase change

*Correspondence authors

Email address: yuying.yan@nottingham.ac.uk (Yuying Yan)

1. Introduction

Energy, Economy and Environment (3E) have the most powerful and urgency importance in current global issues and challenges [1]. Carbon dioxide (CO₂) emissions, both natural and human sources, has been significantly increasing and contributing a major role in greenhouse and global climate change [2]. Around 87% of CO₂ emissions are due to the human sources come from the utilization of fossil fuels coal, natural gas and oil [3]. Nonetheless, the fossil fuels are still the dominant energy sources for power generation with their share increasing 66% in 2005 to 77% in 2050. Therefore, CO₂ emissions would increase by 61% over 2011 levels by 2050 [4]. To minimize the CO₂ emissions, there is the critical need of alternative and sustainable energy resources to reduce the emerging demand of fossil fuels. With the development of nanotechnology, the heat and mass transfer in nanoconned systems such as nanofluid [5, 6] and nano-composites brings novel insight for energy conversion and storage [7, 8] which make a contribution in thermal management applications. The thermal energy storage (TES) systems based on heat storage materials have been used extensively for energy conversion, storage and transportation in thermal management applications of electronic devices, photovoltaic (PV) modules, Li-ion batteries systems etc. [9, 10, 11]. Phase change materials (PCMs) as heat storage materials meet the series of requirements with higher energy storage density with suitable phase transition temperature range, good stability and low supercooling. For effective heat storage and heat transfer using PCMs, the latent-heat and thermal conductivity are the key thermal properties which improve the thermal management efficiency. Organic PCMs exhibit the best heat storage properties but they have low thermal conductivity which reduces the overall thermal response factor, heat transfer rate and efficiency. Thus, a PCM with higher latent-heat and thermal conductivity with stable chemical structure is the most suitable. To overcome this issue, researchers have introduced several heat transfer enhancement techniques including extruded metal-fins [12, 13, 14, 15, 16, 17], metal-foam and porous materials [18, 19], nanomaterials [20, 21, 22] encapsulated micro/nano-capsules [23, 24, 25, 26]. Many researchers are working on different mechanisms for the thermal controllability of structures. Moreover, in addition to PCM there are some other materials that can be used for thermal management system as well as for energy harvesting systems having applications in mechanical and aerospace engineering [27, 28]. Nanomaterials as a supportive materials into the PCMs have taken keen attention in current era due their higher thermal properties and enhance the chemical and thermal stability. For instance, Babapoor et al. [29, 30]

34 synthesised the composite PCMs using SiO_2 , Al_2O_3 , Fe_2O_3 , ZnO nanoparticles and mea-
35 sured the thermophysical properties. They achieved the highest thermal conductivity with
36 8 wt.% of Fe_2O_3 nanoparticles. However, the authors suggested that Al_2O_3 nanoparticles
37 were preferable for thermal management applications. Nourani and his co-authors [31, 32]
38 prepared NCPCMs using Al_2O_3 nanoparticles of weight concentrations of 0.5, 5, 7.5, and
39 10 wt.% and SSL used as a surfactant to enhance the stability of Al_2O_3 nanoparticles in
40 paraffin wax. The effective thermal conductivity enhancement ratios were found of 31%
41 and 13% in solid and liquid phases, respectively, at 10.0 wt.%. Chieruzzi et al. [33] syn-
42 thesised the mono and hybrid composite PCMs of potassium nitrate (KNO_3), used as a
43 PCM, by adding SiO_2 , Al_2O_3 and hybrid of $\text{SiO}_2/\text{Al}_2\text{O}_3$ having 1.0 wt.%. The best results
44 were obtained with SiO_2 nanoparticles with a decrease of 2 – 3°C in onset temperatures
45 and 9.5% increase in specific heat. Sharma et al. [34] used the TiO_2 nanoparticles of weight
46 concentrations of 0.5, 1.0, 3.0, and 5.0 wt.% and palmitic acid as a PCM to prepare the
47 NCPCMs. The highest thermal conductivity and lowest heat of fusion were obtained of
48 0.35 W/m.K and 180.03 kJ/kg, respectively, at 5.0 wt.% of TiO_2 . Yang et al. [35] prepared
49 the paraffin and palygorskite mixed composite PCM and revealed the melting temperature
50 and latent heat of 54–56°C and 132.18 J/g, respectively. Li et al. [36] synthesised the
51 NCPCMs using calcium chloride hexahydrate ($\text{CaCl}_2\cdot 6\text{H}_2\text{O}$) as a PCM with $\gamma\text{-Al}_2\text{O}_3$ and
52 measured the phase-change thermal properties. The maximum thermal conductivity was
53 obtained of 1.373 W/m.K at 2.0 wt.% of $\gamma\text{-Al}_2\text{O}_3$ nanoparticles. Sami and Etesami [37]
54 prepared the NCPCMs of using TiO_2 and paraffin with mass fractions of 0.5, 0.7, 1, 2, 3
55 and 4 wt.% with and without SSL used as a surfactant. Results explored the optimum con-
56 centration of 3 wt.% of TiO_2 nanoparticles with the 47.8% increase in thermal conductivity
57 with SSL compared to the pure paraffin. Further, authors suggested that addition of SSL
58 in NCPCMs showed the better dispersion and thermal stability compared with pure paraf-
59 fin and TiO_2 /paraffin composite. Bashar and Siddiqui [38] prepared the NCPCMs using
60 various types of nanoparticles, Ag, CuO, Al_2O_3 and MWCNTs and added in paraffin wax.
61 A higher heat transfer coefficient of 18% and 14% was obtained for CuO and Ag nanopar-
62 ticles, respectively, compared with pure paraffin wax. Praveen and Suresh [39] prepared
63 the composite PCMs using solid–solid neopentyl glycol (NPG) and CuO nanoparticles for
64 thermal management application. It was found that maximum thermal conductivity and
65 phase change enthalpy of 0.61 W/m.K and 112.4 kJ/kg, respectively, were obtained at 3.0
66 wt.% of CuO. Recently, Li et al. [40] synthesized MgO dispersed in eutectic carbonate salt

67 of NaLiCO_3 and studied the thermal properties of light and heavy weight MgO nanopar-
68 ticles. The results found that light weight MgO nanoparticles of particle size $3 - 5 \mu\text{m}$
69 had the maximum thermal conductivity of $\sim 5.5 \text{ W/m.K}$ compared to heavy weight MgO
70 nanoparticles of similar size.

71 The literature reveals that most of the studies focused on the development of NCPCMs used
72 for the high temperature TES applications. The current study focuses on synthesising of
73 new NCPCMs which will be the most suitable for thermal management of electronic devices,
74 PV modules and Li-ion batteries, working under the safe and reliable operating tempera-
75 ture range of $30 - 40^\circ\text{C}$ [9, 41]. In addition, the literature indicates that a very little work
76 has been performed on mono and hybrid NCPCMs. Therefore, the present study aims to
77 improve on the thermophysical properties of a commercially available PCM to enhance the
78 thermal performance. The microstructure, chemical and thermal properties are investigated
79 of TiO_2 , Al_2O_3 , and CuO nanoparticles dispersed mono and hybrid NCPCMs. Further, var-
80 ious characterization techniques were adopted to analysis the surface morphology, chemical
81 and physical interaction, thermal properties including phase-change temperature, melt-
82 ing/solidifying latent-heat enthalpies, specific heat capacity, thermal conductivity, thermal
83 stability and reliability. The newly developed NCPCMs were then poured in a heat sink
84 to investigated the transient temperature thermal response to explore the thermal cooling
85 performance.

86 **2. Experimental procedure and characterizations**

87 *2.1. Materials*

88 In present study, the RT-35HC (a commercial grade of paraffin) was used as a PCM with
89 phase-transition temperature of $34 - 36^\circ\text{C}$, purchased from Rubitherm GmbH, Germany.
90 Three different metallic-oxide nanoparticles such as copper oxide (CuO) (particle size < 50
91 nm, surface area: $29 \text{ m}^2/\text{g}$), aluminium oxide (Al_2O_3) (particle size 13 nm , surface area:
92 $85 - 115 \text{ m}^2/\text{g}$), nano Titanium (IV) dioxide (TiO_2), anatase powder (particle size < 25
93 nm, surface area: $45 - 55 \text{ m}^2/\text{g}$, density: 3.9 g/mL at 25°C) were purchased from Sigma-
94 Aldrich, UK. In all samples Sodium dodecylbenzene sulfonate (SDBS) was used, obtained
95 from Sigma-Aldrich, UK. Table 1 is summarized the thermophysical properties of RT-35HC.
96 All materials were used as they received without further chemical treatment.

Table 1: *Thermophysical properties of RT-35HC.*

Melting temperature (°C)	Thermal conductivity (W/m.K)	Latent-heat of fusion (J/kg.K)	Specific heat (J/kg.K)	Density (kg/m ³)
34-36	0.2	240,000	2000	880 (solid) 770 (liquid)

97 2.2. Preparation of nanocomposite PCMs

98 The schematic diagram of preparation of NCPCMs is shown in Figure 1. A well-precise
99 two-step preparation method was carried out to synthesize the mono and hybrid NCPCMs,
100 which has been used extensively in preparation of nanofluids [42]. The RT-35HC was used a
101 base PCM and TiO₂, Al₂O₃ and CuO nanoparticles were used as an additives. The purpose
102 of adding the nanoparticles is to enhance the thermal properties. In first part of NCPCMs
103 preparation, the RT-35HC was melted at a temperature of 70°C constantly through a hot-
104 water bath. The SDBS was then added, as a surfactant, into the RT-35HC at fully melted
105 stage with a ratio of 4:1 wt.% of nanoparticles to enhance the dispersion stability. The
106 nucleating agent mixture of RT-35HC and SDBS was stirred vigorously at 450 rpm and
107 kept for 30 min at 70°C. Thereafter, constant amount of 1.0 wt.% of TiO₂, Al₂O₃, CuO and
108 Al₂O₃+CuO were added separately into RT-35HC and stirring was continued for further 3
109 hrs to achieve a uniform and stable dispersion of nanoparticles. The mass ratio for hybrid
110 NCPCMs was kept 75%/25% of 1.0 wt.% to keep the total mass percentage constant. In
111 second part of the NCPCMs preparation, the ultrasonication process was carried out for
112 60 min at ultrasonic frequency of 40 kHz [8, 43]. The ultrasonication process improved the
113 stable dispersion of nanoparticles more homogeneously and minimized the sedimentation
114 and aggregation, as shown in Figure 2. The four different samples of the mono and hy-
115 brid NCPCMs were prepared and labelled as NCPCM_{TiO₂}, NCPCM_{Al₂O₃}, NCPCM_{CuO} and
116 NCPCM_{Al₂O₃+CuO}. Lastly, samples of NCPCMs were cooled to the ambient temperature.

117 3. Characterizations techniques

118 3.1. Microstructural and chemical interaction analysis

119 An environmental scanning electron microscopy (ESEM, FEI Quanta-650) attached
120 with the energy-dispersive X-ray spectroscopy (EDX) system was employed to examine
121 the surface morphology, microstructure and to visualize the surface elemental distribution of
122 nanoparticles in NCPCMs. Fourier-transform infrared spectroscopy (FTIR, Bruker Tensor-
123 27) was used to record the absorption spectra between the wave range of 400 – 4000 cm⁻¹ at

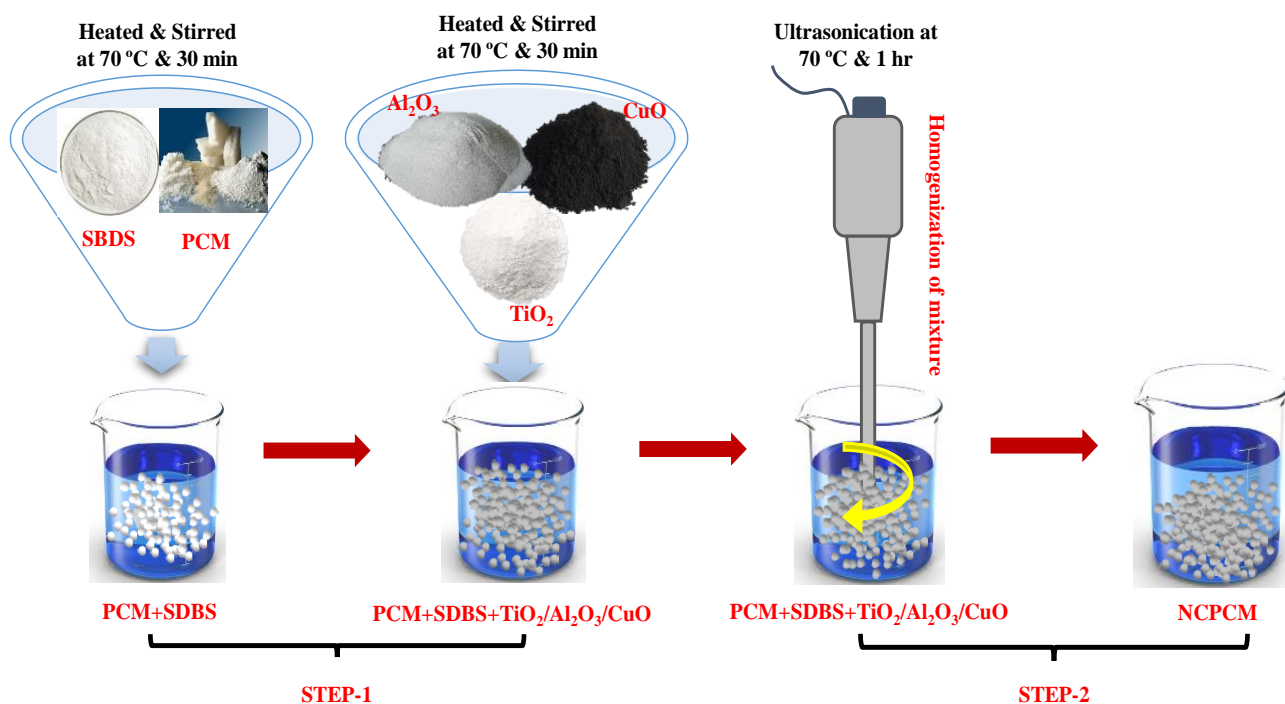


Figure 1: Schematic diagram of synthesizing of TiO_2 , Al_2O_3 , CuO and RT-35HC based mono and hybrid NCPCMs.

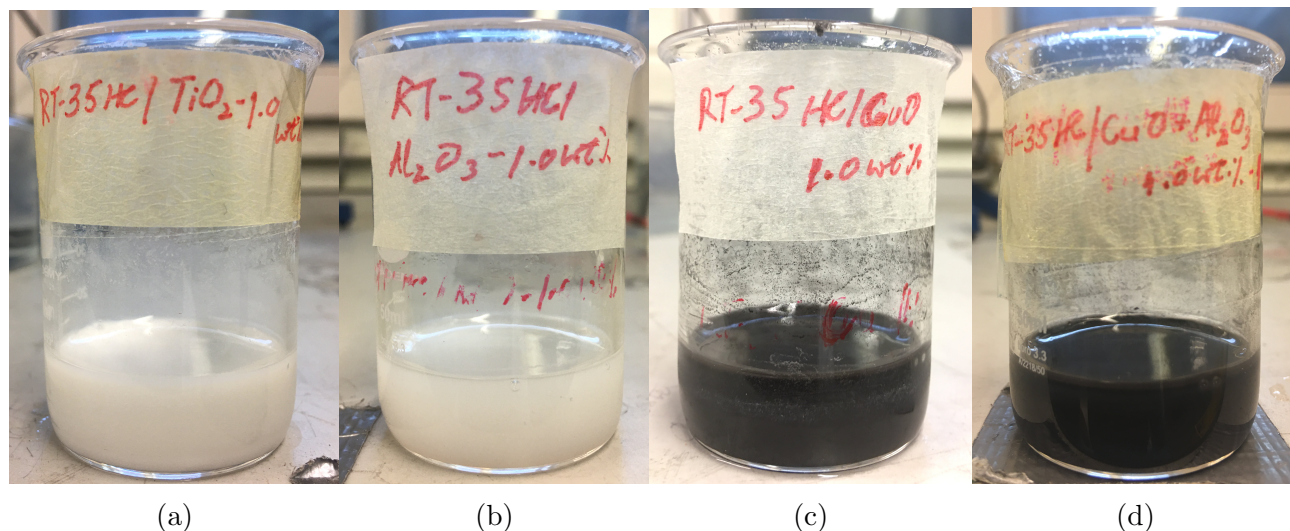


Figure 2: NCPCMs after sonication : (a) $\text{NCPCM}_{\text{TiO}_2}$, (b) $\text{NCPCM}_{\text{Al}_2\text{O}_3}$, (c) $\text{NCPCM}_{\text{CuO}}$, (d) $\text{NCPCM}_{\text{Al}_2\text{O}_3+\text{CuO}}$.

124 room temperature with the spectral resolution of 4 cm^{-1} and wavenumber accuracy of 0.01
 125 cm^{-1} to study the chemical composition and functional groups of NCPCMs. X-ray diffrac-
 126 tometer (XRD, Bruker D8 Advance with Da Vinci) was used to measure the XRD pattern
 127 of NCPCMs with the 2θ angle range of $5\text{--}60^\circ$ with a monochromatic $\text{Cu-K}\alpha$ radiation (λ

128 = 1.5406 Å).

129 3.2. Thermophysical properties analysis

130 The TGA/DSC (SDT-Q600 TA instrument Inc., UK) (error $\pm 0.1 \mu\text{g}$) [44] was used
131 to perform the thermogravimetric analysis (TGA) and derivative thermogravimetry (DTG)
132 analysis of NCPCMs to measure the rate of weight loss and decomposition to address the
133 thermal stability of NCPCMs. The aluminium pan was used filled with sample mass of
134 4 – 7 mg and heating rate was kept at $10^\circ\text{C}/\text{min}$ for a range of $20\text{--}400^\circ\text{C}$ under purified
135 nitrogen purging of 100 mL/min flow rate. Differential scanning calorimeter (DSC-2500,
136 TA instrument Inc., UK) [45] was used to measure the phase transition thermal properties
137 of NCPCMs. The heating and cooling rate was kept of $1^\circ\text{C}/\text{min}$ for a range of $10\text{--}50^\circ\text{C}$.
138 The specific heat capacity was measured of all samples using sapphire method (ASTM-
139 E1269) at a heating rate of $3^\circ\text{C}/\text{min}$ between temperature 10°C and 50°C . The calorimeter
140 has the accuracy of $\pm 0.04\%$ with temperature precision of $\pm 0.005^\circ\text{C}$. The TCiTM thermal
141 conductivity analyser (TCA) (C-THERM Technologies Ltd. Canada) was used to measure
142 the thermal conductivity of RT-35HC and NCPCMs adopting a modified transient plane
143 source (MTPS) method (ASTM-D7984) [46]. The thermal conductivity was measured as
144 function of temperature from 20°C and 55°C . For each sample, at a constant temperature,
145 five measurements were taken and averaged was reported and maximum uncertainty in
146 measurement was obtained of $\pm 1.0\%$. An IR thermographic camera (FLIR-SC2600-EA2)
147 was used to perform the infrared thermography (IRT) tests to obtain the thermal images of
148 samples. The samples were filled immersed in a water pot and constant temperature was
149 provided through the hot-plate.

150 3.3. Thermal cooling performance analysis

151 The experimental setup to perform the thermal cooling performance analysis was car-
152 ried out using a passive cooling thermal management system, as shown in Figure 3. The
153 schematic diagram shows that thermal management system consists mainly the heat sink,
154 data acquisition system, DC power supply and the laptop. The heat sink assembly consists
155 of plate type silicon rubber heater (OMEGALUX), K-type thermocouples (OMEGA), rub-
156 ber mat for insulation, perspex sheet to visualize the physical melt fractions of RT-35HC
157 and NCPCMs. In the experimental set up, the heat sink assembly was perfectly insulated
158 using a rubber pad, having very low thermal conductivity. The rubber pad was placed at

159 the bottom and around the heat sink with a 50 mm extended width/thickness of the ac-
160 tual dimensions of heat sink. A constant temperature was measured at the outside of the
161 insulation during the experiment which was the same with environment room temperature.
162 The top surface of the heat sink was covered with acrylic sheet having a thickness of 5 mm
163 by keeping silicon gasket which prevent the PCM leakage, to visualize the physical melt
164 front of molten PCM. A copper made heat sink was manufactured using computer numer-
165 ical control (CNC) machine. Pure RT-35HC and NCPCMs were poured inside the heat
166 sink. To ensure the proper stability, reduce the aggregation and uniform distribution of
167 nanoparticles, each sample of NCPCMs was sonicated before pouring into the heat sink.
168 A DC power supply made of Keysight Technologies (N6700C, 0.5 A/100 V) was used to
169 provide different power levels of 3-5 W at ambient temperature, to mimic heat generation.
170 A PC based digital data acquisition system (Agilent 34972A, USA) was used to record the
171 temperature variation through thermocouples inserted at different points on the heat sink.
172 The data acquisition system was connected to the laptop and Agilent Technologies, Inc.
173 (Taft Ave. Loveland, USA) software is used to record the temperature at interval of 5 s
174 during the experimentation. The uncertainty of the measured quantities is associated with
175 the least count of the corresponding measurement devices. The uncertainty in temperature
176 measurement according to according to ASTM standard [47] in a temperature range of 0–
177 100°C with maximum variation of $\pm 0.1^\circ\text{C}$. The uncertainty in data logger is $\pm 0.1^\circ\text{C}$. The
178 uncertainties in voltage and current are measured of ± 0.01 V and ± 0.001 A, respectively.
179 The uncertainty in heat input are calculated using Kline and McClintock [48] technique and
180 minimum and maximum uncertainties are obtained of 1.68% and 1.91%, respectively.

181 4. Results and discussions

182 4.1. ESEM and EDX analysis

183 The microstructure and surface morphology of mono and hybrid NCPCMs analysed by
184 the ESEM are presented in Figure 4. The surface microstructural features of NCPCM_{TiO₂},
185 NCPCM_{Al₂O₃}, NCPCM_{CuO} and NCPCM_{Al₂O₃+CuO} are presented in Figure 4a, 4b, 4c, 4d,
186 4e, 4f, 4g and 4h of LFD and BSED images, respectively. It can be seen from Figure 4
187 that the dispersion of nanoparticles in RT-35HC is uniform representing in white regions
188 which is due to the repulsive bonding of the dispersing agent. Since the loading of nanopar-
189 ticles is constant and very less despite the fact, all nanoparticles are well dispersed and

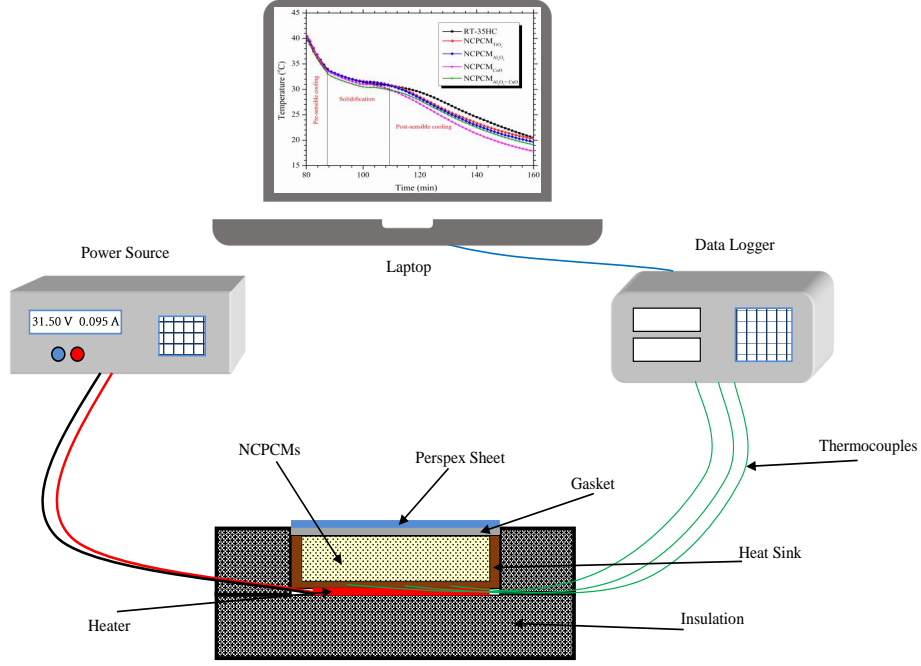


Figure 3: Schematic diagram of experimental setup.

190 embedded enough to show their presence in NCPCMs. Besides, the homogenous and het-
 191 erogeneous percolation of nanoparticles in RT-35HC can be observed from LFD and BSED
 192 images. From Figure 4, the presence of zones characterized by the heterogeneous aggregates
 193 of nanoparticles and RT-35HC can be observed clearly. Similar observations of nanopar-
 194 ticles percolation in NCPCMs have been reported in Ref. [29, 30, 33]. While solid-liquid
 195 phase transition of NCPCMs, the solvation, “Brownian motion” and “electrostatic repul-
 196 sion” cause the nanoparticles to separate individually. However, this collision becomes more
 197 prominent between the nanoparticles by increasing the loading of the nanoparticles and Van
 198 der Waals force becomes stronger at a short range resulting in the formation of aggregates
 199 and sedimentation of nanoparticles at high concentration. Therefore, the uniform dispersion
 200 and percolation of nanoparticles depend on the size of the nanoparticles.

201 The EDX maps of $\text{NCPCM}_{\text{TiO}_2}$ and $\text{NCPCM}_{\text{Al}_2\text{O}_3+\text{CuO}}$ are shown in Figure 5 and 6, respec-
 202 tively. Figure 5a, 5b and 5c show the distribution of carbon (C), oxygen (O) and titanium
 203 (Ti) elements, respectively, present in $\text{NCPCM}_{\text{TiO}_2}$. The presence of all elements C, Ti and
 204 O in different colours can be seen in single image of TiO_2 dispersed $\text{NCPCM}_{\text{TiO}_2}$ in Figure 5d.
 205 The EDX mapping of carbon (C), oxygen (O), aluminium (Al), and copper (Cu) elements
 206 of hybrid $\text{NCPCM}_{\text{Al}_2\text{O}_3+\text{CuO}}$ can be seen in Figure 6a, 6b, 6c and 6d, respectively. Figure 6e
 207 shows the presence of all C, Al, Cu and O elements in various colours in $\text{NCPCM}_{\text{Al}_2\text{O}_3+\text{CuO}}$.

208 The ESEM and EDX images show the smaller zones of agglomeration of nanoparticles. The
209 similar observations have been reported in previous studies [33, 34]. Consequently, it is
210 recommended that for more better and uniform dispersion of the nanoparticles in PCM, the
211 smaller size, low density and higher surface area nanoparticles are preferable [49, 50].

212 4.2. FT-IR analysis

213 The chemical composition and structural interaction of TiO_2 , Al_2O_3 and CuO dispersed
214 NCPCMs were characterized by FT-IR spectroscopy. Figure 7 presents the FT-IR spectrum
215 of nanoparticles, RT-35HC and NCPCMs and absorption peaks were observed. For instance,
216 the three absorption peaks at 2955 cm^{-1} , 2913 cm^{-1} , 2849 cm^{-1} represent the medium C-H
217 symmetrical and anti-symmetrical stretching vibration of methyl ($-\text{CH}_3$) and methylene
218 ($-\text{CH}_2-$) group. The peak at 1472 cm^{-1} identifies the medium C-H scissoring of $-\text{CH}_2-$ and
219 deformation of antisymmetric stretching vibration $-\text{CH}_3$ group in RT-35HC. The FT-IR
220 spectrum also shows a series of absorption peaks at 1371 , 1125 , and 891 cm^{-1} which are
221 due to the C-H bending and scissoring vibrations. The peak at 715 cm^{-1} represents to
222 the weak rocking vibration of C-H in long-chain methyl group. The FT-IR spectrum of
223 TiO_2 shows the two peaks around 510 and 526 cm^{-1} which are attributed to the Ti-O
224 stretching vibrations in TiO_2 . In case of CuO , there are two stretching bands at 880 cm^{-1}
225 and 1432 cm^{-1} which represent the characteristics bands of Cu-OH functional group [51, 52].
226 Furthermore, there is a small peak can be observed at 729 cm^{-1} which indicates the standard
227 adsorption spectra pattern of the amorphous structure or disordered defects of $\gamma\text{-Al}_2\text{O}_3$. It
228 can be revealed that both mono and hybrid NCPCMs presented the consistent peaks with
229 that of the pure RT-35HC which means that NCPCMs contained similar characteristics of
230 pure RT-35HC without emergence of new peak or any peak shift. This means that there
231 no considerable chemical interaction occurred between the TiO_2 , Al_2O_3 and CuO and RT-
232 35HC and there is only physical interaction which indicate that prepared mono and hybrid
233 NCPCMs are chemical stable.

234 4.3. XRD analysis

235 The crystallography analysis of TiO_2 , Al_2O_3 , CuO , RT-35HC and NCPCMs were iden-
236 tified through XRD patterns to study the crystalline phase and dimensions of unit cell, , as
237 shown in Figure 8. The diffraction peaks of 2θ at 25.3° (101), 37.79° (004), 48.03° (200),
238 53.88° (105) and 55.06° (211) confirm the anatase form of the TiO_2 (PDF No. 03-065-5714).
239 The peaks of Al_2O_3 confirmed the presence of γ -phase of Al_2O_3 nanoparticles at $2\theta = 19.50^\circ$

240 (013), 32.80° (022), 34.60° (117), 36.76° (122), 39.50° (026) and 45.64° (220) with PDF No.
241 00-046-1131. The diffraction peaks at $2\theta = 32.50^\circ$ (110), 35.54° (111), 38.70° (111), 46.26°
242 (112), 48.71° (202), 53.48° (020), and 58.26° (202) confirmed the CuO (PDF No. 01-073-
243 6023). The sharp diffraction peaks of pure RT-35HC was observed at 6.85° (002), 10.48°
244 (003), 13.91° (004), 17.44° (005), 19.32° (010), 19.80° (011), 20.83° (012), 22.43° (013),
245 23.32° (105), 24.78° (-101), 25.65° (110), 28.12° (008), 31.75° (009), 34.75° (-110), 35.27°
246 (0010), 39.83° (0-22), 42.73° (0012), 44.60° (207), 52.68° (220), 53.41° (-2-14) and 57.55°
247 (-205) which attributed to the crystal planes of *n-eicosane* ($C_{20}H_{42}$) with PDF No. 00-045-
248 1543. As the loading of TiO_2 , Al_2O_3 and CuO was kept constant of 1.0 wt.%, a less amount
249 of nanoparticles dispersed in pure RT-35HC. Consequently, less significant physical changes
250 were observed in mono and hybrid NCPCMs. The XRD results revealed that the crystalline
251 phase of RT-35HC did not alter, further both mono and hybrid NCPCMs samples contain
252 the peaks of TiO_2 , Al_2O_3 and CuO.

253 4.4. TGA and DTG analysis

254 Figure 9 presents the thermal gravimetric analysis of RT-35HC and hybrid NCPCMs to
255 investigate their thermal stability. The thermal stability of NCPCMs is estimated on the
256 onset temperature of PCM degradation and rate of weight loss at which is occurs. The TGA
257 and DTG curves show the one-step and two-step thermal degradation process, respectively.
258 The TGA curves of RT-35HC and NCPCMs, shown in Figure 9a, represent that there is no
259 distinguishable weight loss in any sample up to $\sim 120^\circ C$. The rate of weight loss increases
260 with the increase of temperature and reaches at the maximum degradation temperature with
261 constant residual. For RT-35HC, the initial disintegration starts at $217.70^\circ C$ and maximum
262 degradation temperature is $255.01^\circ C$ with 1.85% charred residue. While decomposition pro-
263 cess, caused by the evaporation of pure RT-35HC, the hydrocarbon chains breakdown into
264 monomers ($CH_3CH:CH+CH_4$). The onset decomposition and maximum degradation tem-
265 peratures of all samples are summarized in Table 2 and in case of hybrid $NCPCM_{Al_2O_3+CuO}$,
266 the charred residue was 3.62% at $262.78^\circ C$ and remained constant subsequently. In NCPCMs,
267 the nanoparticles create the protective layer on the surface of RT-35HC which delays the
268 vaporization of RT-35HC during the thermal degradation. The DTG curves of RT-35HC
269 and NCPCMs are shown in Figure 9b and revealed that addition of nanoparticles have
270 improved the thermal stability, because no decompositions was observed in samples until
271 $\sim 150^\circ C$. Thus, hybrid $NCPCM_{Al_2O_3+CuO}$ can effectively be used for thermal management

272 systems. The improvement in thermal stability can be explained by the following reasons:
 273 (i) *the onset decomposition temperature is related to the specific heat capacity of NCPCMs*
 274 *which can be raised by the specific heat capacity of nanoparticles* and (ii) *enhanced thermal*
 275 *conductivity of NCPCMs which can transfer heat faster and uniformly within the PCM* [53].

Table 2: *The temperature changes and residue of TiO_2 , Al_2O_3 , CuO and RT-35HC based mono and hybrid NCPCMs.*

Sample	Onset decomposition temperature (°C)	Maximum-rate degradation temperature (°C)	Residue (%)
RT-35HC	217.70	255.01	1.85
NCPCM $_{TiO_2}$	226.77	263.55	1.96
NCPCM $_{Al_2O_3}$	225.24	264.07	4.01
NCPCM $_{CuO}$	228.37	264.57	6.04
NCPCM $_{Al_2O_3+CuO}$	224.87	262.78	3.62

276 4.5. DSC analysis

277 DSC analysis presents the phase-transition temperatures and latent-heat of melting/solidification
 278 of NCPCMs, as shown in Figure 10. Figure 10a and 10b present the endothermic and
 279 exothermic curves, respectively, of RT-35HC and NCPCMs and measured values of phase-
 280 transition thermal properties are summarized in Table 3. It can be seen that the addition
 281 of nanoparticles have slightly changed the thermal properties of RT-35HC after synthesiz-
 282 ing. The latent-heat of melting/solidification of NCPMCs were decreased with the addition
 283 of nanoparticles, as expected. A single endothermic peak is observed of RT-35HC and
 284 NCPCMs during melting, indicating an isomorphous crystalline form of RT-35HC either in
 285 a pristine state or in the NCPCMs one. Contrary, a bimodal crystallization behaviour is
 286 predicted of RT-35HC and NCPCMs by presenting a main exothermic peak temperature
 287 along with an additional peak of higher temperature during solidification process. This two-
 288 phase transitions phenomenon is ascribed by the appearance of a metastable rotator phase
 289 prior to completing the complete crystallization as a results of the heterogeneous nucleation
 290 during the cooling process [8, 54, 55].

291 The comparison of the melting (ΔH_m) and solidification (ΔH_s) enthalpies of RT-35HC and
 292 NCPCMs are presented in Figure 10c. The ΔH_m and ΔH_s of RT-35HC are determined of
 293 255.88 and 260.06 J/g, respectively. The reduction in ΔH_m of NCPCM $_{TiO_2}$, NCPCM $_{Al_2O_3}$,
 294 NCPCM $_{CuO}$ and NCPCM $_{Al_2O_3+CuO}$ has been obtained of 7.83%, 8.24%, 8.59% and 10.72%
 295 as compared to the pure RT-35HC. Similarly, the maximum reduction in ΔH_s latent-
 296 heats are 7.98%, 7.08%, 9.47%, and 11.81% for NCPCM $_{TiO_2}$, NCPCM $_{Al_2O_3}$, NCPCM $_{CuO}$ and
 297 NCPCM $_{Al_2O_3+CuO}$, respectively. The reduction in latent-heats are due to the addition of

nanoparticles and mass fraction (ω) of crystallized RT-35HC in NCPCMs is determined by the Equation 1:

$$\omega = \frac{\Delta H_{NCPCM}}{\Delta H_{PCM}} \times 100 \quad (1)$$

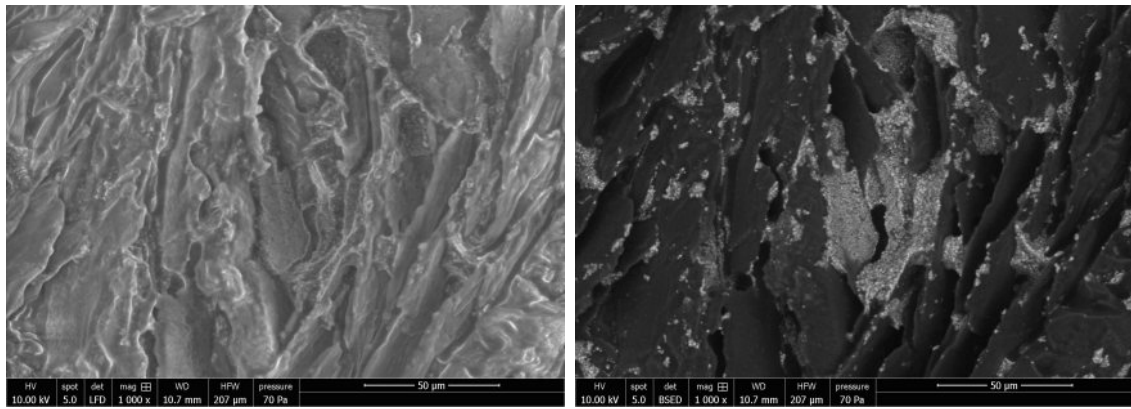
where, ΔH_{NCPCM} and ΔH_{PCM} are the endothermic latent-heat of NCPCM and pure PCM, respectively. While synthesising of NCPCMs, the nanoparticles replace the RT-35HC molecules resulting in reduce the latent-heat capacity of the NCPCMs which lead to the absorption/release of more energy. The degree of super-cooling (ΔT) of NCPCMs is presented in Figure 10d. The peak melting temperature (T_m) and crystallization temperature (T_c) of RT-35HC are determined as 36.09°C and 31.71°C, respectively. The maximum deviations in T_m are determined as -0.30%, -1.14%, -0.97% and -0.08% for NCPCM_{TiO₂}, NCPCM_{Al₂O₃}, NCPCM_{CuO} and NCPCM_{Al₂O₃+CuO}, respectively, compared to the RT-35HC. The slight variations are observed in T_c which are due the crystallization confinement of the nanoparticles surface layers within the NCPCMs. This interfacial surface layers cause to form the imperfect RT-35HC resulting in a slight variation in T_m . These two factors result in an increase in ΔT . The reduction in ΔT for NCPCM_{Al₂O₃+CuO} is obtained of 4.32°C, which shows the better significance hybrid nanoparticles as nucleating agents compared to the mono nanoparticles in terms of its surface adsorption and effective homogeneous nucleation.

Figure 10e illustrates the experimental and calculated latent-heat of fusion for NCPCMs, calculated using Equation 2 [56]:

$$\Delta L_{NCPCM} = \Delta L_{PCM} \cdot \omega = \Delta L_{PCM}(1 - \varphi) \quad (2)$$

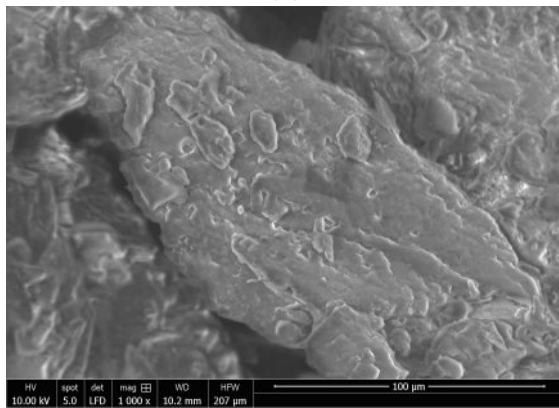
where ΔL_{NCPCM} and ΔL_{PCM} calculated and experimental latent-heat of fusion of NCPCM and PCM, respectively, ω and φ are the mass fraction of PCM and nanoparticles, respectively. It can be revealed that experimental values of latent-heat of fusion of mono and hybrid NCPCMs are lower than the calculated values. The deviation in results is due the type of the nanoparticles, since the loading of all nanoparticles in NCPCMs is constant. The relative error (RE) of experimental and calculated values has been obtained 6 ~ 9% for all NCPCMs, given in Table 3. The similar trend of deviations in experimental and calculated values latent-heat of fusion have reported in Refs. [36, 8, 56]. The results reveal that NCPCM_{Al₂O₃+CuO} has the optimum value of latent-heat which is preferable for thermal

326 management systems. The discrepancies in latent-heat values are because of the surface
327 morphology, structure, size and rate of dispersion of the nanoparticles while synthesising
328 the NCPCMs.

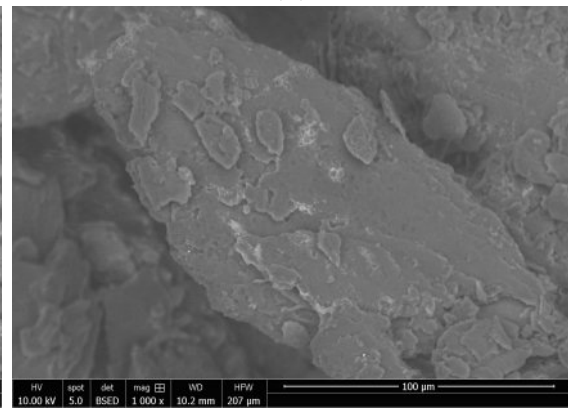


(a)

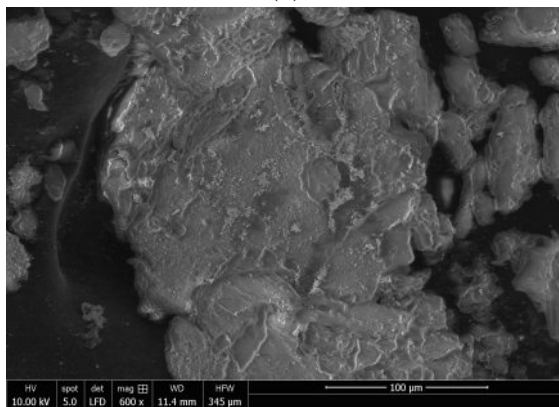
(b)



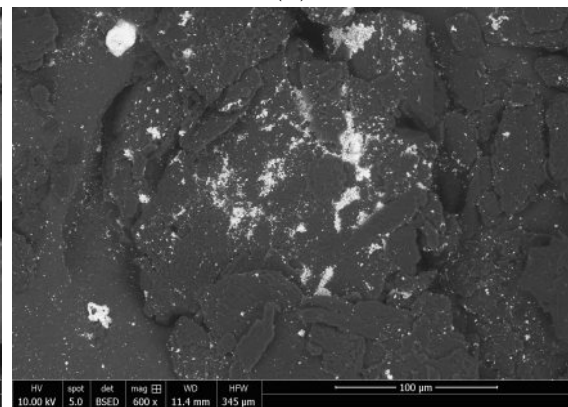
(c)



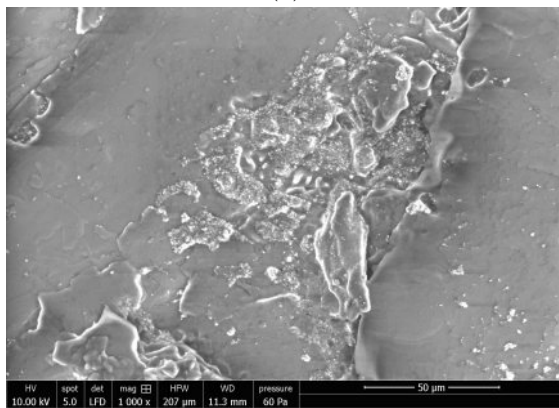
(d)



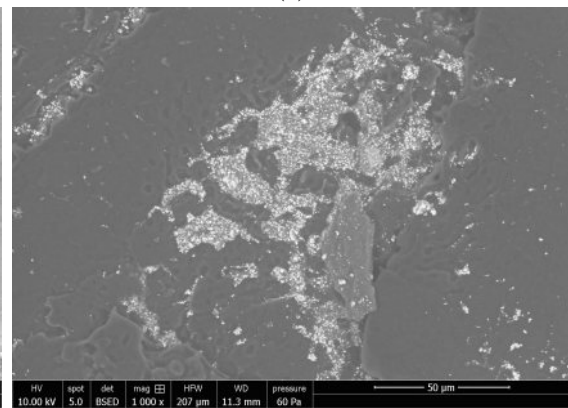
(e)



(f)



(g)



(h)

Figure 4: *ESEM* images of $NCPCM_{TiO_2}$ (a) LFD and (b) BSED, $NCPCM_{Al_2O_3}$ (c) LFD and (d) BSED, $NCPCM_{CuO}$ (e) LFD and (f) BSED, and $NCPCM_{Al_2O_3+CuO}$ (g) LFD and (h) BSED.

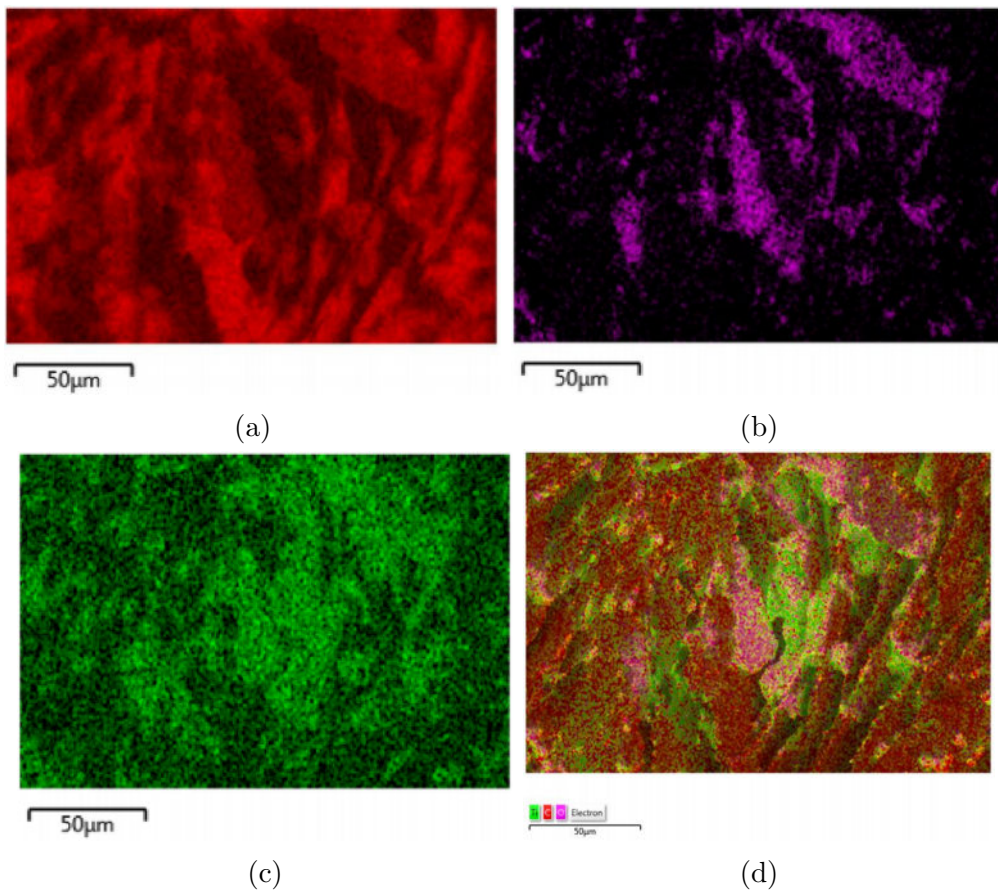


Figure 5: *EDX mapping of $NCPCM_{TiO_2}$ (a) carbon-(red), (b)-oxygen-(purple), (c) Titanium-(green), (d)-EDX map of oxygen, carbon, and titanium elements present in $NCPCM_{TiO_2}$.*

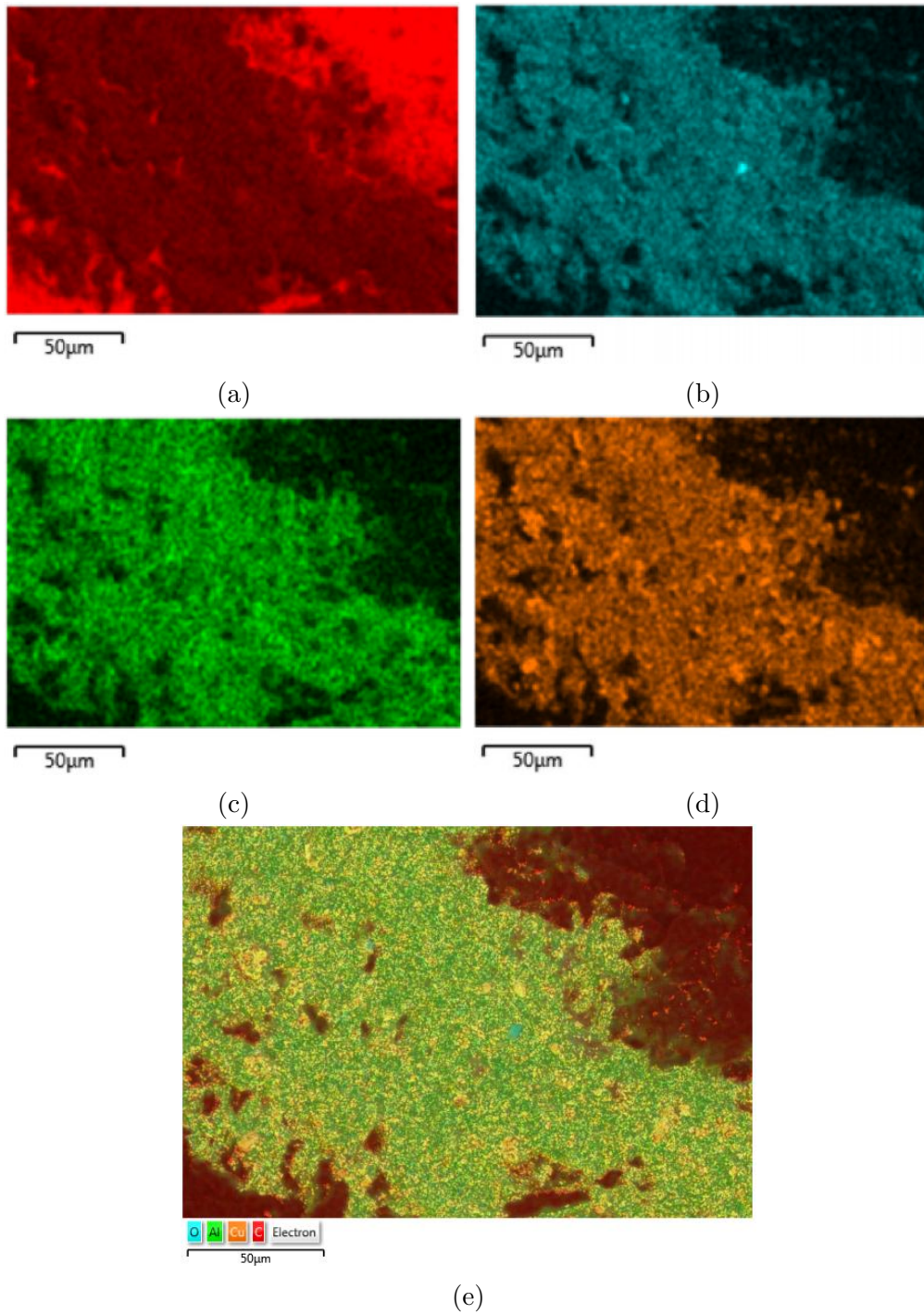


Figure 6: *EDX mapping of $NCPCM_{Al_2O_3+CuO}$ (a) carbon-(red), (b)-oxygen-(cyan), (c) Titanium-(green).*

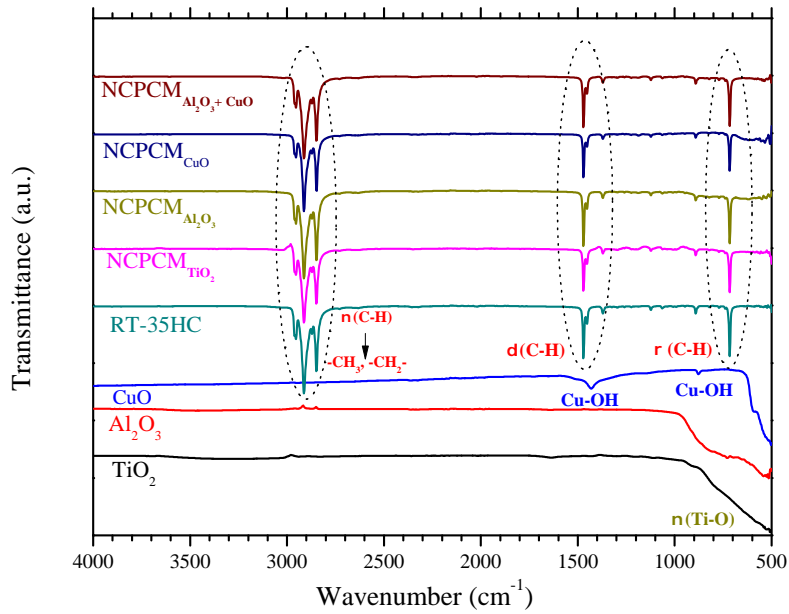


Figure 7: *FT-IR spectrum of TiO_2 , Al_2O_3 , CuO and RT-35HC based mono and hybrid NCPCMs.*

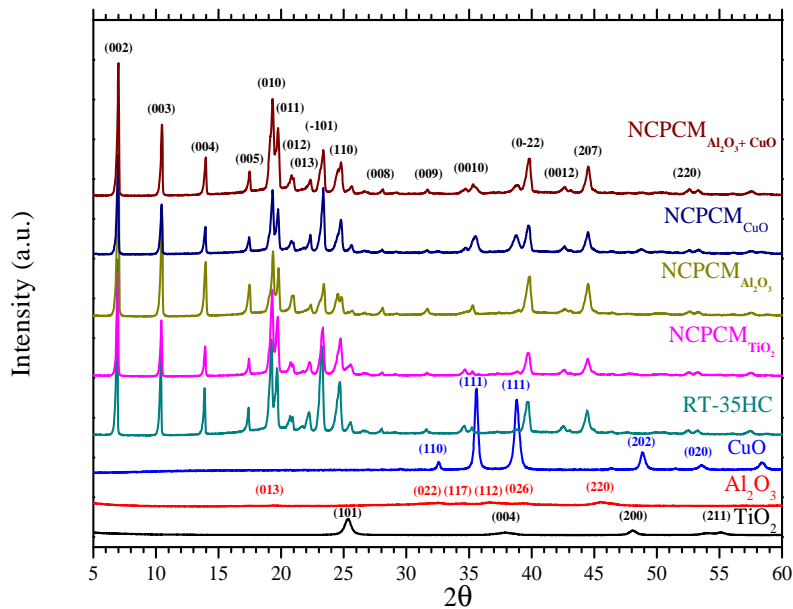


Figure 8: *XRD pattern of TiO_2 , Al_2O_3 , CuO and RT-35HC based mono and hybrid NCPCMs.*

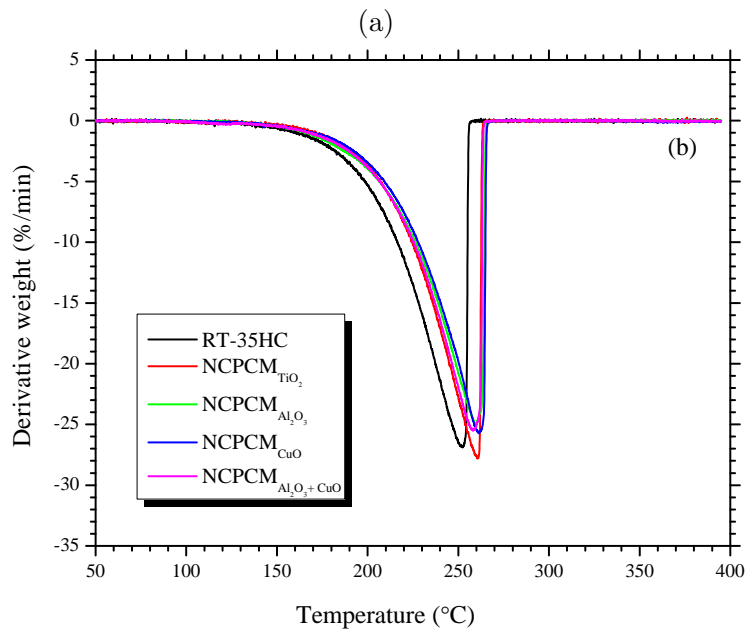
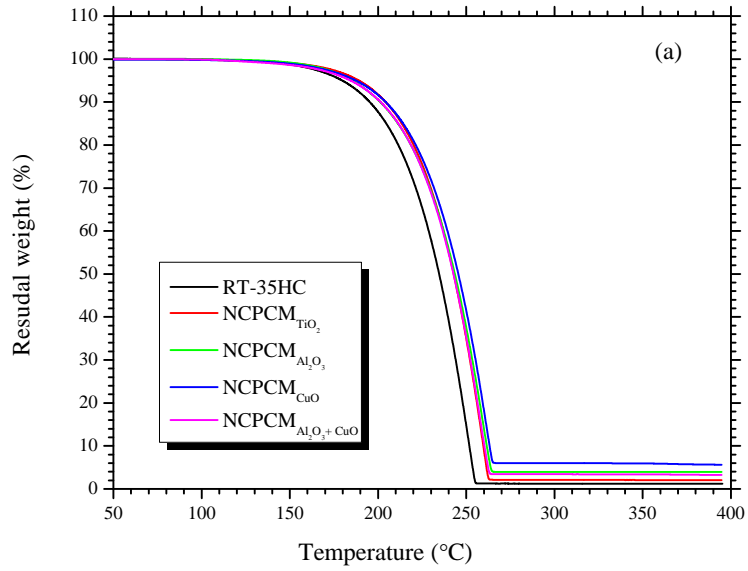


Figure 9: (a)-TGA and (b)- DTG thermograms of TiO_2 , Al_2O_3 , CuO and RT-35HC based mono and hybrid NCPCMs.

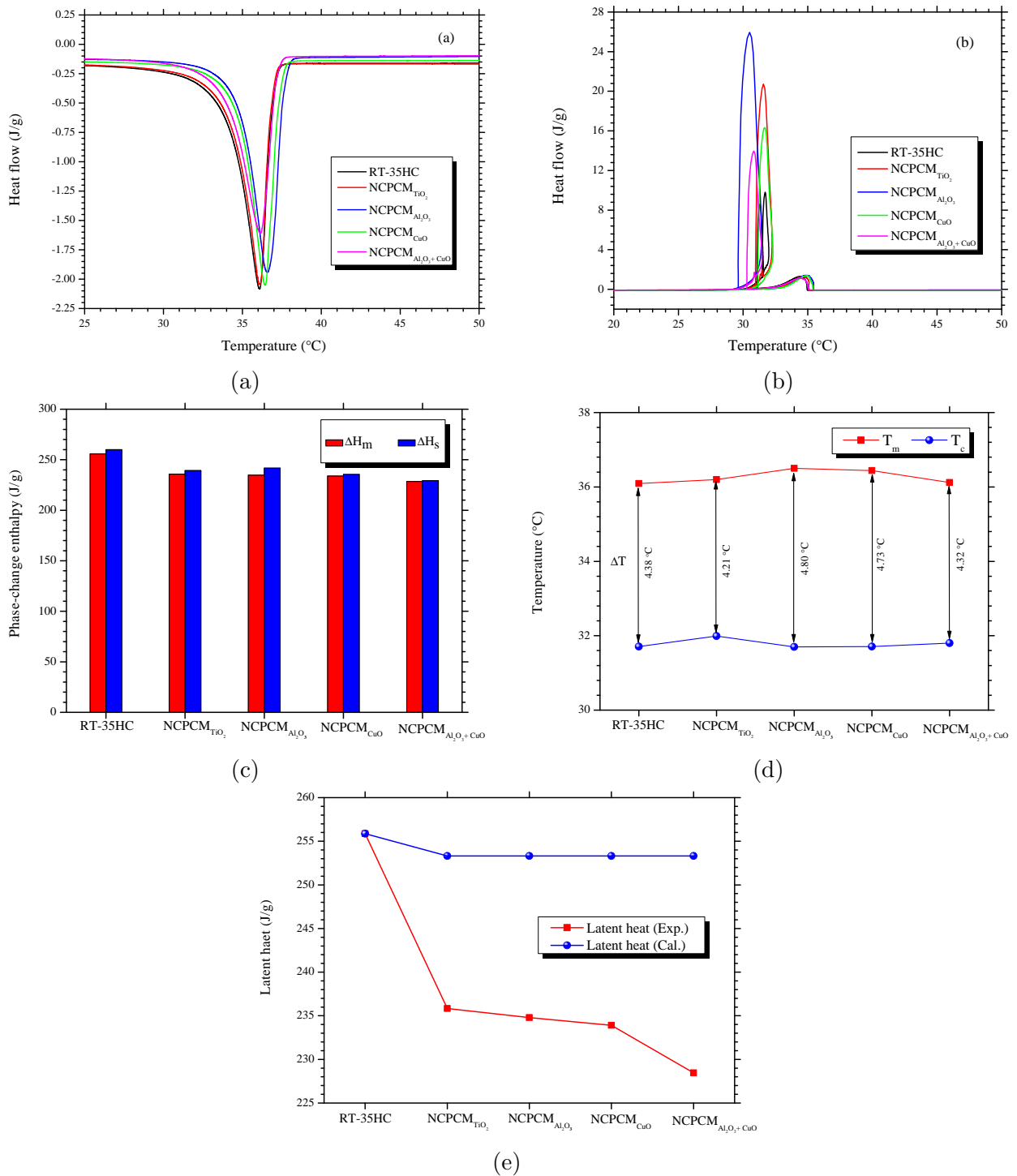


Figure 10: The results of (a) Melting, (b) Solidification curves, (c) Phase-change enthalpies, (d) Degree of super-cooling and (e) Comparison of latent-heats of fusions of TiO_2 , Al_2O_3 , CuO and RT-35HC based mono and hybrid NCPCMs.

Table 3: Phase-change thermal properties of TiO_2 , Al_2O_3 , CuO and RT-35HC based mono and hybrid NCPCMs*.

Sample	Heating					Cooling					ω (%)	ΔT
	$T_{oset,m}$	$T_{peak,m}$	$\Delta H_{m,exp}$	$\Delta H_{m,cal}$	RE (%)	$T_{oset,c}$	$T_{peak,c}$	$\Delta H_{c,exp}$	$\Delta H_{c,cal}$	RE (%)		
RT-35HC	34.06	36.09	255.88	-	-	31.47	31.71	260.79	-	-	100	4.38
NCPCM $_{TiO_2}$	34.26	36.20	235.84	253.32	6.90	31.48	31.99	239.30	257.46	7.05	92.17	4.21
NCPCM $_{Al_2O_3}$	34.76	36.50	234.79	253.32	7.32	29.61	31.70	241.65	257.46	6.14	91.76	4.80
NCPCM $_{CuO}$	34.70	36.44	233.91	253.32	7.66	31.13	31.71	235.42	257.46	8.56	91.41	4.73
NCPCM $_{Al_2O_3+CuO}$	33.87	36.12	228.46	253.32	9.81	30.28	30.82	229.34	257.46	9.81	89.28	4.32

$T_{oset,m}$: Onset melting temperature, $T_{peak,m}$: Peak melting temperature, $\Delta H_{m,exp}$: Experimental latent-heat of melting,
 $\Delta H_{m,cal}$: Calculated latent-heat of melting, $T_{oset,c}$: Onset cooling temperature, $T_{peak,c}$: Peak cooling temperature,
 $\Delta H_{c,exp}$: experimental latent-heat of cooling, $\Delta H_{c,cal}$: Calculated latent-heat of cooling, RE: Relative error,
 ω : Mass percentage of RT-35HC, ΔT : Degree of supercooling

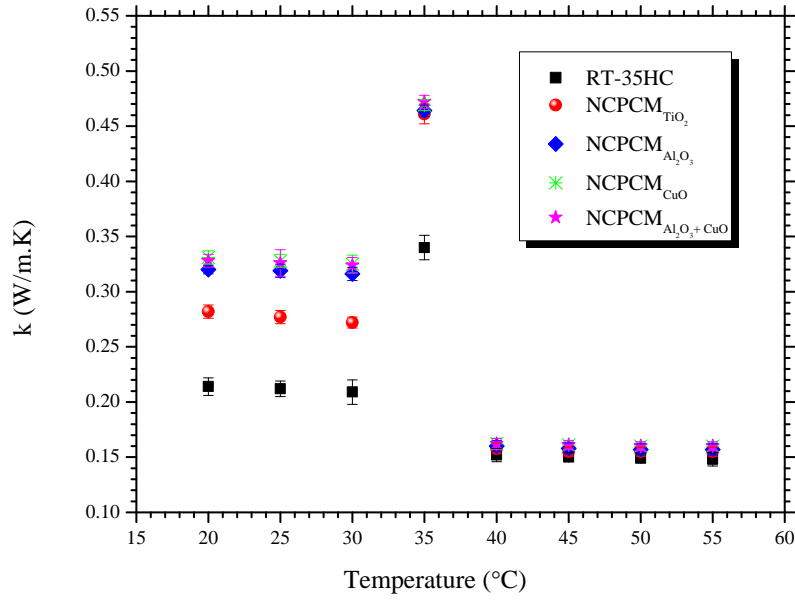
329 4.6. Thermal conductivity measurements

330 Figure 11 presents the results of thermal conductivity (k) and thermal conductivity en-
 331 hancement factor (η) of RT-35HC and NCPCMs. It can be seen that by dispersing the
 332 nanoparticles thermal conductivity generally increases because of the higher thermal con-
 333 ductivity of nanoparticles. The average thermal conductivity of RT-35HC and NCPCMs
 334 is measured for solid-phase (20–30°C), phase-change ($\sim 35^\circ\text{C}$) and liquid-phase (40–55°C)
 335 regions with an increment of 5°C. It can be evidenced that the constant trend is predicted in
 336 enhancement in thermal conductivity in solid and liquid phases. However, a sharp increas-
 337 ing and decreasing behaviour was predicted when the temperature increased from 30°C to
 338 35°C and 35°C to 40°C, respectively. This behaviour reveals that thermal conductivity is
 339 strongly depended on the temperature. The phenomenon of sudden increase and decrease
 340 in thermal conductivity was due to the random motion of molecules within a disordered mi-
 341 crostructure of lattice in liquid-phase. The maximum thermal conductivities of 0.340, 0.464,
 342 0.461, 0.469 and 0.472 W/m.K were obtained at phase-change temperature ($\sim 35^\circ\text{C}$) for
 343 RT-35HC, NCPCM_{TiO₂}, NCPCM_{Al₂O₃}, NCPCM_{CuO} and NCPCM_{Al₂O₃+CuO}, respectively,
 344 shown in Figure 11a. However, the maximum thermal conductivities for solid phase at 20°C
 345 were obtained of 0.214, 0.320, 0.282, 0.331 and 0.328 W/m.K for RT-35HC, NCPCM_{TiO₂},
 346 NCPCM_{Al₂O₃}, NCPCM_{CuO} and NCPCM_{Al₂O₃+CuO}, respectively. The higher thermal con-
 347 ductivities at phase-change temperature ($\sim 35^\circ\text{C}$) is because of the phase-change temper-
 348 ature range 34–36°C at which the NCPCM is in metastable condition. At phase-change
 349 temperature, the crystalline structure of RT-35HC becomes unstable and the increase in
 350 temperature accelerates the molecular vibration of in the lattice, thus thermal conductivity
 351 of RT-35HC and NCPCMs increases dramatically at the melting point ($\sim 35^\circ\text{C}$) [57]. It
 352 can be clearly observed that NCPCM_{Al₂O₃+CuO} has the highest thermal conductivity in all
 353 three phases. Furthermore, the percentage of η of RT-35HC and NCPCMs is shown in
 354 Figure 11b, as given by Equation 3:

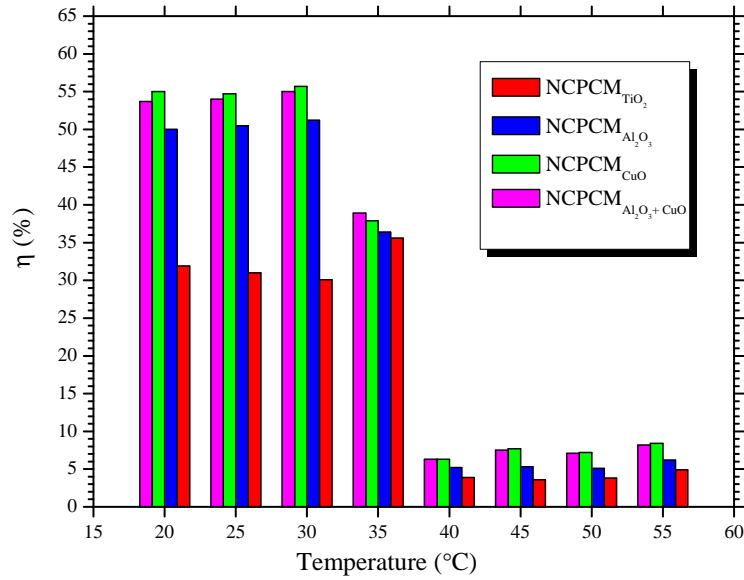
$$\eta = \frac{k_{NCPCM} - k_{PCM}}{k_{PCM}} \times 100 \quad (3)$$

355 where, k_{NCPCM} and k_{PCM} are the thermal a conductivity of NCPCM and pure PCM, re-
 356 spectively.

357 Figure 11b presents an increasing trend in enhancement thermal conductivity are ob-
 358 served with change of temperature. A relative enhancements of 55.0%, 54.0% and 53.7%



(a)



(b)

Figure 11: The results of (a) thermal conductivity and (b) thermal conductivity enhancement factor of TiO_2 , Al_2O_3 , CuO and RT-35HC based mono and hybrid NCPCMs as a function of temperature.

359 are obtained for NCPCM_{Al₂O₃+CuO} at 30°C, 25°C and 20°C, respectively, compared to the
 360 RT-35HC. However, higher percentage enhancement in thermal conductivity is observed
 361 for NCPCM_{CuO} of 55.7%, 54.7% and 55.0% at 30°C, 25°C and 20°C, respectively, compared to the RT-35HC. The higher enhancement in thermal conductivity in case of CuO
 362 nanoparticles is because of higher thermal conductivity of CuO nanoparticles compared to
 363 the hybrid Al₂O₃+CuO nanoparticles. The variations in thermal conductivity results in
 364 case of mono and hybrid NCPCMs are due to the nanoparticles size, morphology, den-
 365

366 sity, thermal conductivity and dispersion stability into the NCPCMs. The Al_2O_3 and TiO_2
 367 nanoparticles have the smaller size and density and higher surface area compared to CuO
 368 nanoparticles. Therefore, they have more stronger degree of homogenization and dispersion
 369 rate into the RT-35HC. Thenceforth, the combination of $\text{Al}_2\text{O}_3+\text{CuO}$ hybrid nanoparti-
 370 cles having different thermophysical properties reveal the finer dispersion stability. Further
 371 more, the boundary layer of thermal resistance of nanoparticles and lattice molecules of
 372 PCM contribute a major factor in variation of thermal conductivity results [58]. Generally,
 373 there exists two major factors that cause the enhanced phenomenon of thermal conductance
 374 within the NCPCMs. Firstly, higher thermal conductivity of the nanoparticles and secondly
 375 the motion of the nanoparticles in NCPCMs in liquid-phase which causes a quasi-convection
 376 phenomenon [29, 8].

377 4.7. Specific heat capacity analysis

378 The specific heat capacity results of RT-35HC and NCPCMs are shown in Figure 12 for
 379 solid and liquid phases as a function of temperature from 10°C to 60°C . Since the specific
 380 heat capacity has the less effect in total thermal energy storage due to low thermal energy
 381 storage density in sensible heat storage phase. Regardless, specific heat capacity influences
 382 additional effects in the total heat stored by a PCM within the storage temperature range
 383 of storage which is calculated using Equation 4 as follows:

$$Q = \int_{T_i}^{T_m} mC_p \cdot dt + m\alpha_m \Delta H_m + \int_{T_m}^{T_f} mC_p \cdot dt \quad (4)$$

384 where, Q (J) is the quantity of total heat stored, T_i ($^\circ\text{C}$), T_m ($^\circ\text{C}$) and T_f ($^\circ\text{C}$) are the initial,
 385 melting and final temperatures, respectively, m (kg) mass of the heat storage medium, C_p
 386 (J/kg.K) is the specific heat capacity, α_m is the faction of melted mass and ΔH_m (J/kg) is the
 387 heat of fusion per unit mass. From Equation 4, it is important to investigate the specific heat
 388 capacity variations with temperature to analysis heat transfer and heat storage performance.

389 The specific heat capacity of NCPCMs increases gradually with temperature between
 390 14°C to 30°C in solid-phase (Figure 12a) while it remains constant in liquid-phase (Figure
 391 12b). The presented results of specific heat capacity of both phases showed the good agree-
 392 ment with the previous studies [33, 59, 60]. The specific heat capacities of RT-35HC for solid
 393 and liquid phases are obtained of 1.88 and 1.77 J/g $^\circ\text{C}$, respectively. It can be revealed that
 394 with addition of the nanoparticles, the specific heat capacity of NCPCMs increases both in
 395 solid and liquid phases. The higher values of specific heat capacities are obtained of 2.61 and

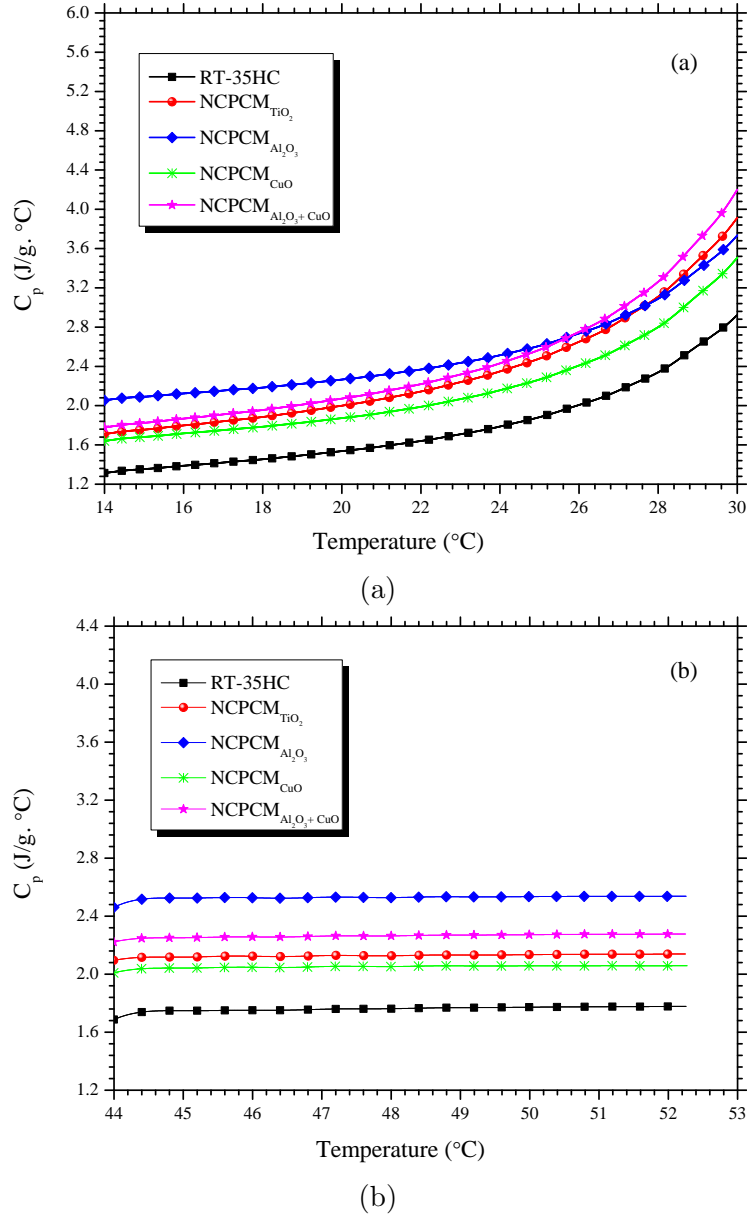


Figure 12: Specific heat capacity curves of TiO_2 , Al_2O_3 , CuO and RT-35HC based mono and hybrid NCPCMs: (a) solid-phase (b) liquid-phase.

396 2.53 $J/g \cdot ^\circ C$ at 25 $^\circ C$ and 50 $^\circ C$, respectively, for NCPCM_{Al₂O₃}. The polynomial equations are
 397 generated for RT-35HC and NCPCMs for solid-phase after fitting the experimental data
 398 mentioned in Equation 5 and coefficients are given in Table 4.

$$C_p = AT^3 + BT^2 + CT + D \quad (5)$$

399 Figure 13 represents the comparison of the comparison of specific heat capacities for RT-
 400 35HC and NCPCMs for 25 $^\circ C$ and 50 $^\circ C$ for solid and liquid phases, respectively. Figure 15a
 401 shows that variations in specific heat capacity are significantly depends on the type and spe-
 402 cific heat capacity of the nanoparticles. Additionally, the nanoparticles size, density, surface

403 area and morphology contribute the most prominent effects in enhancement in specific heat
 404 capacity. The specific heat capacity enhancement factor (ζ) is calculated using Equation 6
 405 to evaluate the effect of nanoparticles in enhancement of specific heat capacity:

$$\zeta = \frac{C_{P_{NCPCM}} - C_{P_{PCM}}}{C_{P_{PCM}}} \times 100 \quad (6)$$

406 where, $C_{P_{NCPCM}}$ and $C_{P_{PCM}}$ are the specific heat capacity of the NCPCM and PCM, respec-
 407 tively. The maximum enhancements are obtained of 38.62% is achieved for $NCPCM_{Al_2O_3}$,
 whereas it is 36.47% for $NCPCM_{Al_2O_3+CuO}$ in solid phase compared to the RT-35HC.

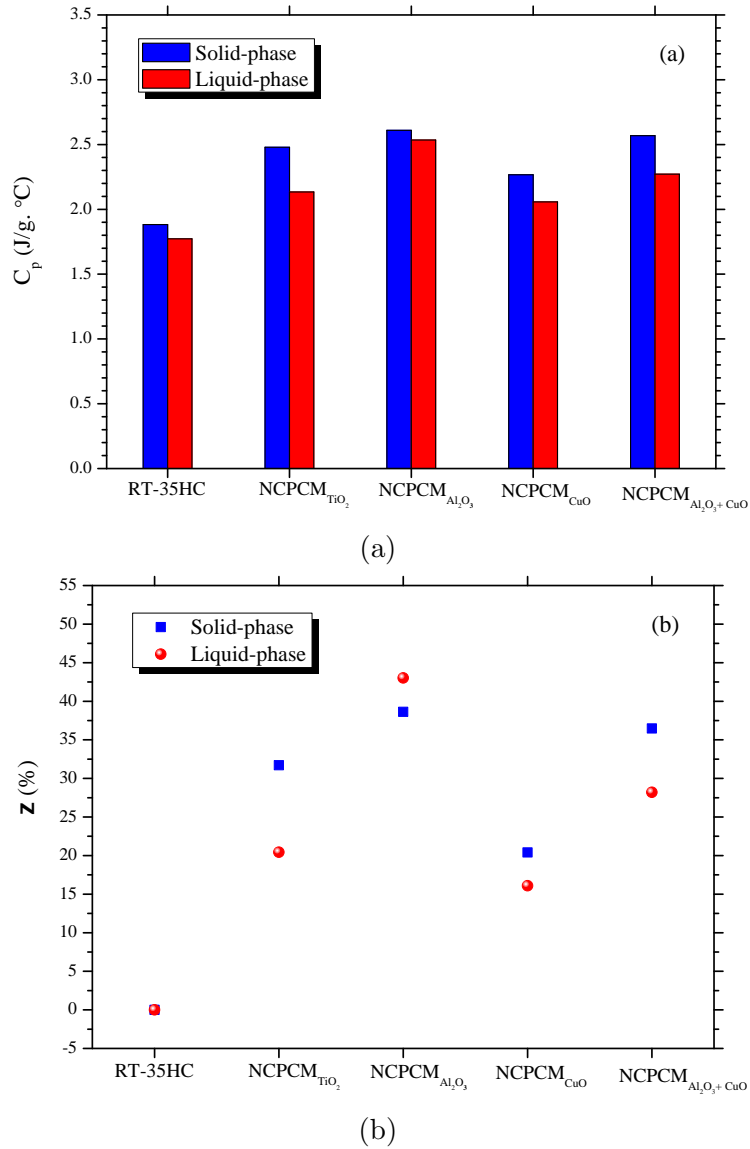


Figure 13: (a) Comparison of specific heat capacity, (b) specific heat capacity enhancement of TiO_2 , Al_2O_3 , CuO and RT-35HC based mono and hybrid NCPCMs.

408
 409 The enhancement in specific heat capacity is associated with the following reasons: (i)
 410 an enhanced anharmonicity of the atomic interaction due to their volume expansion, (ii)

Table 4: *Coefficients of the third-order polynomials in solid-state, C_p ($J/g \cdot ^\circ C$).*

	A	B	C	D	R ²
RT-35HC	0.0006	-0.0349	0.6687	-2.9832	0.9988
NCPCM _{TiO₂}	0.0008	-0.0457	0.8701	-3.8549	0.9987
NCPCM _{Al₂O₃}	0.0007	-0.0397	0.7606	-2.8072	0.9981
NCPCM _{CuO}	0.0008	-0.0425	0.8092	-3.5154	0.9985
NCPCM _{Al₂O₃+CuO}	0.0010	-0.0567	1.0825	-5.1234	0.9981

411 impurities [61], (iii) the grain boundaries of nanosized materials which possess an excess
412 volume with respect to the perfect crystal lattice and (iv) the high specific surface energies
413 related to the high surface area of the nanoparticles per unit volume [62, 63]. In addition, the
414 morphology of the nanoparticles also influences significantly, since the smaller size nanopar-
415 ticles provide the larger interfacial surface area per unit mass between solid nanoparticles
416 and surrounding material, thus increase the contribution of interfacial effects in the suspen-
417 sion [64, 65, 66]. The interfacial interaction of solid-solid or solid-liquid may alter phonon
418 spectrum or phonon vibration mode of nanoparticles near the surface area and therefore,
419 change the specific heat capacity of NCPCM [67]. The high specific surficial interface area of
420 nanoparticles can adsorb liquid molecules to its surface which form the liquid layers. These
421 liquid layers constrain the nanoparticles and alter their free-boundary surface atoms into
422 the non-free interior atoms [62, 67]. Therefore, the variation in specific heat capacity of
423 NCPCMs is because of the varied Gibbs free energy of the nanoparticles and liquid layers.

424 4.8. IRT analysis

425 The IR thermographic images of mono and hybrid NCPCMs are shown in Figure 14
426 which presents the surface temperature distribution during the melting process at different
427 time steps. The melting stages of NCPCM_{Al₂O₃}, NCPCM_{CuO} and NCPCM_{Al₂O₃+CuO} can
428 be seen clearly at each time step, labelled as (X), (Y) and (Z), respectively, as shown in
429 Figure 14a. The change in temperature of mono and hybrid NCPCMs can be observed from
430 the temperature scale which indicates the lower to higher temperature variations from blue
431 to red colours, respectively. The uniform melting of each sample is observed while heating
432 at constant temperature. The quick flow away and shrinkage is observed in NCPCM_{CuO},
433 shown in 14f. This phenomenon during phase change from solid-to-liquid causes to lose its
434 shape-stability completely. In case of hybrid NCPCM_{Al₂O₃+CuO}, uniform phase transition
435 is observed with slight shrinkage and flow away due to the heating-impact effect. Since,
436 the NCPCMs only contain the 1 wt.% of Al₂O₃+CuO, therefore only slight shrinkage is

437 observed. It has been reported that the flow away and shrinkage level decrease with the
438 increase of the loading of nanoparticles. The melting process of NCPCM_{Al₂O₃+CuO} shows
439 that it does not melt completely till at 35 min and surface temperature of hybrid NCPCM
440 is lower than the mono NCPCM. This reveals that the best heat transfer performance due
441 to thermal properties and thermal stability. The enhancement in hybrid NCPCM_{Al₂O₃+CuO}
442 is due to the uniform and homogeneous dispersion of Al₂O₃ and CuO nanoparticles in RT-
443 35HC, which increase the viscosity and shape-stability. Moreover, the thermographic images
444 of NCPCM_{Al₂O₃+CuO} shows the enhanced latent-heat phase duration and uniform natural
445 convection heat transfer which can be used in thermal management systems for electronics.

446

447 4.9. Transient thermal analysis

448 The transient thermal analysis was carried out by investigating the melting and cooling
449 processes of pure RT-35HC and NCPCMs, as shown in Figure 15 at a power level of 4
450 W. All samples were poured into a copper made heat sink after sonication to ensure the
451 homogeneous dispersion of nanoparticles. The purpose of using the heat sink in current
452 study, was to investigate the real time thermal response of NCPCMs compared to pure
453 PCM. Since the heat sink has been widely used as heat exchanger that transfers the heat
454 generated inside the electronics towards the ambient through a fluid medium. RT-35HC
455 and NCPCMs were used as fluid medium inside the heat sink as passive cooling medium.

456 4.9.1. Melting process

457 The melting curves of RT-35HC, NCPCM_{TiO₂}, NCPCM_{Al₂O₃}, NCPCM_{CuO} and NCPCM_{Al₂O₃+CuO}
458 are shown in Figures 15a. It can be seen from melting process that there is rapid increase of
459 temperature linearly in all samples up to the first 20min without showing any phase change.
460 Heat transfer occurs in sensible heat transfer mode because of temperature gradient and
461 specific heat capacity of the samples before melting starts. In addition, the heat transfer
462 depends on the thermal conductivity of the samples. The quicker heating rate was observed
463 for NCPCMs because of higher thermal conductivity. Since the loading content is constant
464 in each sample, thus the variation in average heat sink base temperature is very small. Spe-
465 cific heat capacity of each sample also contribute a major role in total heat transfer rate.
466 In second stage, NCPCMs started melting and a large amount of heat was absorbed be-
467 cause of latent-heat of fusion. Thus, the heat sink base temperature increased slowly which
468 eventually enhanced the thermal performance of NCPCMs based heat sink, used for passive

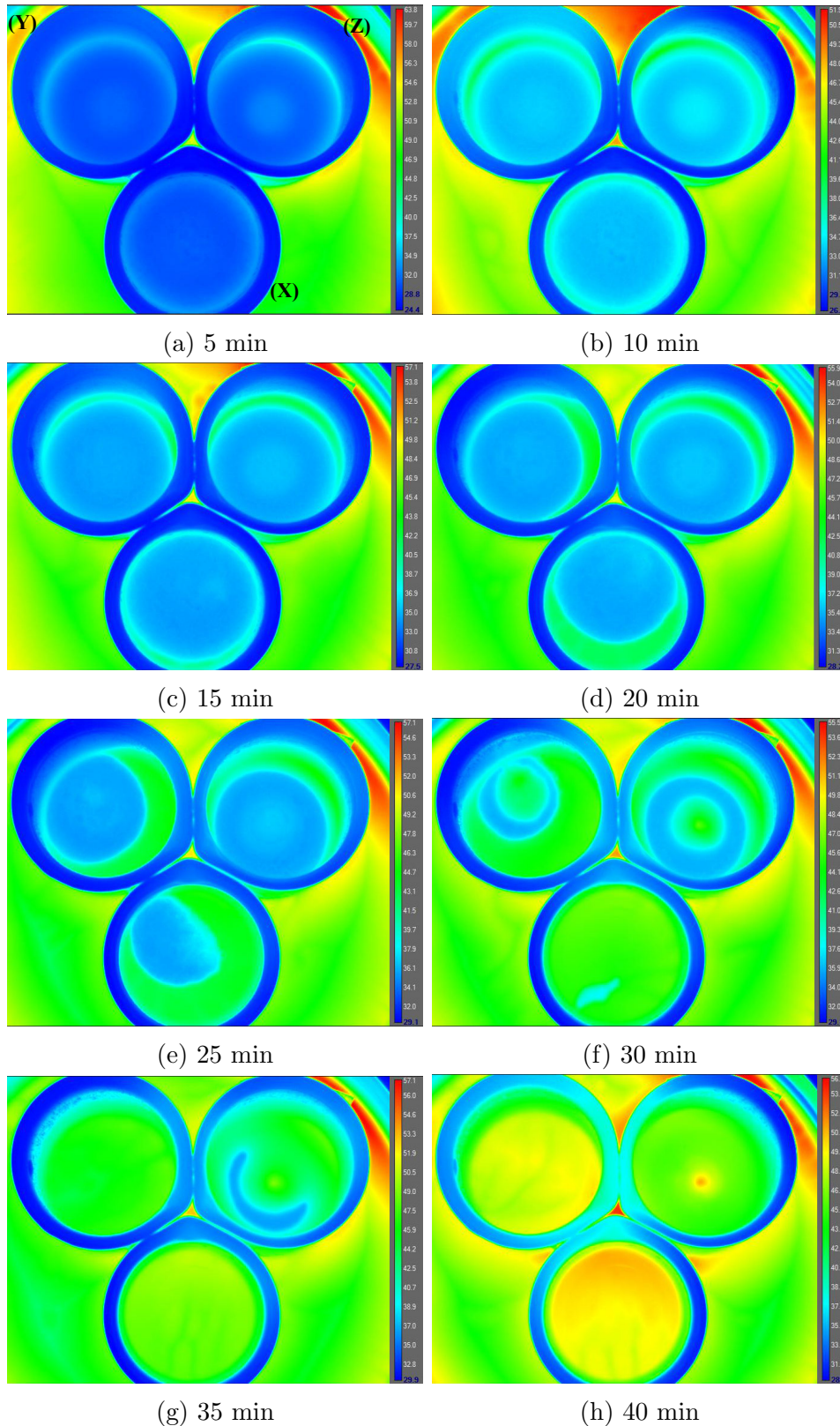


Figure 14: *IRT images of the melting process of $NCPCM_{Al_2O_3}$ -(X), $NCPCM_{CuO}$ -(Y) and $NCPCM_{Al_2O_3+CuO}$ -(Z) at different time steps with temperature variation in $^{\circ}C$.*

469 cooling of electronic devices. The viscosity of composite PCM increases directly by adding
 470 the nanoparticles along with thermal conductivity. The optimum heat transfer and storage

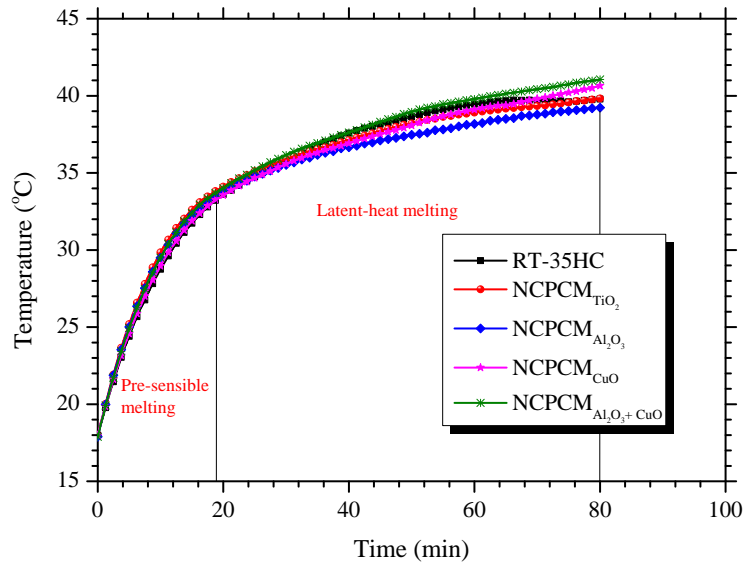
471 of composite PCM also depends on the viscosity of NCPCMs at loading content of 1.0wt.%.
472 The lower temperature rise of heat sink base is beneficial for the thermal management of
473 electronic devices, Li-ion battery and PV modules.

474 4.9.2. Cooling process

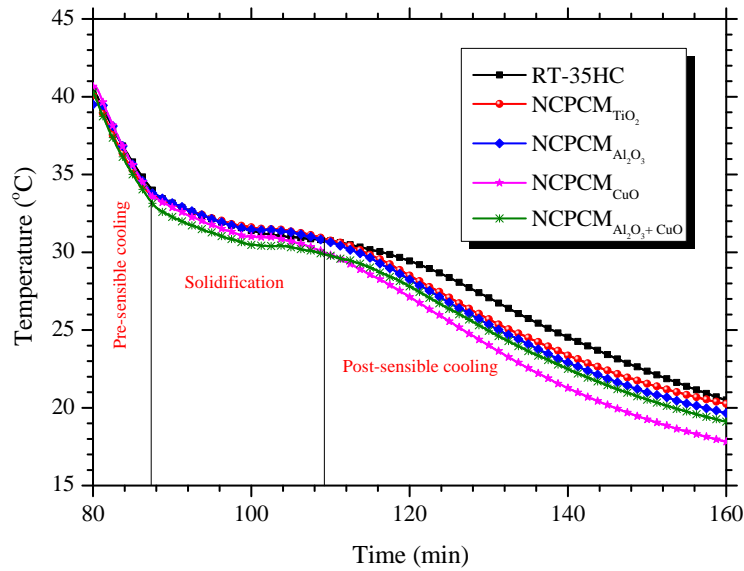
475 The cooling curves of RT-35HC, NCPCM_{TiO₂}, NCPCM_{Al₂O₃}, NCPCM_{CuO} and NCPCM_{Al₂O₃+CuO}
476 are shown in Figure 15b. The transient temperature variation of heat sink base tempera-
477 ture can be divided into three different stages: pre-sensible cooling, latent-heat of solidifi-
478 cation and post-sensible cooling. It can be observed closely that NCPCMs have the faster
479 decrement in temperature compared to the pure PCM. The higher rate of temperature
480 decrease reflects the higher thermal conductivity enhancement of NCPCMs due the addi-
481 tion of TiO₂, Al₂O₃, CuO nanoparticles. During the cooling process, the base temperature
482 decreased sharply and NCPCMs released their sensible heat to cool down up to their con-
483 gealing temperature. Further, the NCPCMs started solidifying process due to their latent-
484 heat of solidification at ambient temperature through natural convection phenomenon. The
485 minimum temperatures of 22.36°C, 21.54°C, 20.99°C, 19.24°C and 20.52°C were recorded
486 for RT-35HC, NCPCM_{TiO₂}, NCPCM_{Al₂O₃}, NCPCM_{CuO} and NCPCM_{Al₂O₃+CuO}, respec-
487 tively, after 150 min of cooling process. The reduction in heat sink base temperature was
488 achieved of 3.67%, 6.13%, 13.95% and 8.23% for NCPCM_{TiO₂}, NCPCM_{Al₂O₃}, NCPCM_{CuO}
489 and NCPCM_{Al₂O₃+CuO}, respectively, compared to RT-35HC. It can be observed that cool-
490 ing process was longer than the melting process. Also, phase change process of PCM and
491 NCPCMs was more prolonged while cooling process than the melting process. The reason
492 behind of such irregular melting and cooling phenomenon depends on the heating/cooling
493 rate. While cooling process, the melting rate was higher than the cooling process which
494 took the less time to change the solid-liquid phase than the cooling process while phase
495 transition from liquid to solid phase. The results revealed that the addition of nanoparticles
496 improve the cooling rate of PCM result in decrease the average temperature heat sink base.
497 Thus, NCPCMs filled heat sink improves the cooling efficiency and enhance the reliability
498 of electronic devices.

499 5. Conclusions

500 The current experimental study explores the physical, chemical and thermal properties
501 of metallic oxide nanoparticles (TiO₂, Al₂O₃ and CuO) based nanocomposite phase change



(a)



(b)

Figure 15: (a) Melting process and (b) solidifying process of TiO_2 , Al_2O_3 , CuO and RT-35HC based mono and hybrid NCPCMs.

502 materials (NCPCMs). Material characteristic techniques such as ESEM, FT-IR, TGA,
 503 DSC and TCA were used to investigate optimum thermal properties for efficient thermal
 504 management systems and solar thermal energy storage. The critical findings are summarized
 505 as follows:

- 506 • The surface morphological analysis of ESEM revealed the uniform dispersion and
 507 presence of TiO_2 , Al_2O_3 and CuO nanoparticles in RT-35HC. Furthermore, XRD
 508 patterns confirmed the presence of all the nanoparticles in both mono and hybrid
 509 NCPCMs.

- 510 • The FT-IR spectrum presents that there is no chemical interaction between the
511 nanoparticles and RT-35HC, and no peak shifting was observed. Hence, there is
512 only physical interaction of TiO_2 , Al_2O_3 and CuO nanoparticles with RT-35HC.
- 513 • The TGA and DTG analysis explored that all mono and hybrid NCPCMs did not
514 loss the chemical and thermal stability. In fact, the addition of TiO_2 , Al_2O_3 and
515 CuO nanoparticles improved the thermal and chemical stability of RT-35HC. More-
516 over, the hybrid $\text{NCPCM}_{\text{Al}_2\text{O}_3+\text{CuO}}$ showed the better stability than mono NCPCMs
517 ($\text{NCPCM}_{\text{TiO}_2}$, $\text{NCPCM}_{\text{Al}_2\text{O}_3}$ and $\text{NCPCM}_{\text{CuO}}$).
- 518 • Overall, the phase-change enthalpy of melting/solidification was decreased with the
519 addition of TiO_2 , Al_2O_3 and CuO nanoparticles in both mono and hybrid NCPCMs.
520 The latent-heat of melting of 235.84, 234.79, 233.9 and 228.46 J/g were obtained for of
521 $\text{NCPCM}_{\text{TiO}_2}$, $\text{NCPCM}_{\text{Al}_2\text{O}_3}$, $\text{NCPCM}_{\text{CuO}}$ and $\text{NCPCM}_{\text{Al}_2\text{O}_3+\text{CuO}}$, respectively. Simi-
522 larly, the latent-heat of solidification of 239.30, 241.65, 235.4 and 229.34 were obtained
523 for of $\text{NCPCM}_{\text{TiO}_2}$, $\text{NCPCM}_{\text{Al}_2\text{O}_3}$, $\text{NCPCM}_{\text{CuO}}$ and $\text{NCPCM}_{\text{Al}_2\text{O}_3+\text{CuO}}$, respectively.
524 The maximum deviation in peak melting temperatures were observed of -1.14% for
525 $\text{NCPCM}_{\text{Al}_2\text{O}_3}$ and hybrid $\text{NCPCM}_{\text{Al}_2\text{O}_3+\text{CuO}}$ showed the deviation of -0.08% .
- 526 • The thermal conductivity result predicted that hybrid $\text{NCPCM}_{\text{Al}_2\text{O}_3+\text{CuO}}$ mass per-
527 centage ratio of 75%/25% showed the maximum thermal conductivity of 0.328 W/m.K
528 with thermal conductivity enhancement of 53.7% compared to RT-35HC.
- 529 • The increasing trend in the specific heat capacity of NCPCMs were observed. The
530 maximum enhancements were obtained of 38.62% for $\text{NCPCM}_{\text{Al}_2\text{O}_3}$, whereas it was
531 36.47% for hybrid $\text{NCPCM}_{\text{Al}_2\text{O}_3+\text{CuO}}$ in solid phase compared to the pure RT-35HC.
532 However, the enhancement in specific heat capacity depends on the nanoparticles size,
533 type, density, surface area and morphology of the nanoparticles.
- 534 • The uniform melting and temperature distribution were observed from IR thermo-
535 graphic images of mono and hybrid NCPCMs. The enhancement in melting time
536 was obtained with hybrid $\text{NCPCM}_{\text{Al}_2\text{O}_3+\text{CuO}}$ because of uniform dispersion of Al_2O_3
537 and CuO nanoparticles having varying densities and particle sizes. The reduction
538 in heat sink base temperature was achieved of 3.67%, 6.13%, 13.95% and 8.23% for
539 $\text{NCPCM}_{\text{TiO}_2}$, $\text{NCPCM}_{\text{Al}_2\text{O}_3}$, $\text{NCPCM}_{\text{CuO}}$ and $\text{NCPCM}_{\text{Al}_2\text{O}_3+\text{CuO}}$, respectively, com-
540 pared to RT-35HC.

541 The current study finally concludes that newly synthesized metallic oxide nanoparticles
542 based hybrid NCPCMs have the better improvement in the thermal energy storage prop-
543 erties compared to the mono NCPCMs, which ultimately enhance the rate of heat transfer
544 in conjugate heat transfer mode. Thereby, hybrid NCPCMs can be successfully used in
545 passive thermal management systems for electronic devices, Li-ion batteries, photovoltaics
546 modules and direct utilization in solar thermal energy storage and distribution in natural
547 environment.

548 **6. Acknowledgement**

549 This research is facilitated by the Faculty of Engineering, University of Nottingham, UK
550 research infrastructure. The first author (Adeel Arshad) acknowledges the University of
551 Nottingham for awarding him the *Faculty of Engineering Research Excellence PhD Schol-*
552 *arship* to pursue a Ph.D. research program. The authors acknowledge the use of facilities
553 at Nanoscale and Microscale Research Centre of the University of Nottingham supported
554 by Engineering and Physical Sciences Research Council [grant number EP/L022494/1].

555 **References**

- 556 [1] F. Bosselman, J. B. Eisen, J. Rossi, D. B. Spence, J. L. Weaver, Energy, economics
557 and the environment: cases and materials, ENERGY, ECONOMICS AND THE EN-
558 VIRONMENT: CASES AND MATERIALS, Foundation Press.
- 559 [2] R. Quadrelli, S. Peterson, The energy–climate challenge: Recent trends in CO2 emis-
560 sions from fuel combustion, Energy Policy 35 (11) (2007) 5938–5952. doi:10.1016/j.
561 enpol.2007.07.001.
- 562 [3] F. Jotzo, P. J. Burke, P. J. Wood, A. Macintosh, D. I. Stern, Decomposing the 2010
563 global carbon dioxide emissions rebound, Nature Climate Change 2 (4) (2012) 213–214.
564 doi:10.1038/nclimate1450.
- 565 [4] O. Akashi, T. Hanaoka, T. Masui, M. Kainuma, Halving global GHG emissions by 2050
566 without depending on nuclear and CCS, Climatic Change 123 (3-4) (2013) 611–622.
567 doi:10.1007/s10584-013-0942-x.
- 568 [5] L. Shi, Y. Hu, Y. He, Magneto-responsive thermal switch for remote-controlled loco-
569 motion and heat transfer based on magnetic nanofluid, Nano Energy 71 (2020) 104582.
570 doi:10.1016/j.nanoen.2020.104582.
- 571 [6] L. Shi, Y. Hu, Y. Bai, Y. He, Dynamic tuning of magnetic phase change composites
572 for solar-thermal conversion and energy storage, Applied Energy 263 (2020) 114570.
573 doi:10.1016/j.apenergy.2020.114570.
- 574 [7] L. Shi, X. Wang, Y. Hu, Y. He, Investigation of photocatalytic activity through photo-
575 thermal heating enabled by fe₃o₄/TiO₂ composite under magnetic field, Solar Energy
576 196 (2020) 505–512. doi:10.1016/j.solener.2019.12.053.
- 577 [8] A. Arshad, M. Jabbal, Y. Yan, Preparation and characteristics evaluation of mono
578 and hybrid nano-enhanced phase change materials (NePCMs) for thermal management
579 of microelectronics, Energy Conversion and Management 205 (2020) 112444. doi:
580 10.1016/j.enconman.2019.112444.
- 581 [9] A. R. M. Siddique, S. Mahmud, B. V. Heyst, A comprehensive review on a passive
582 (phase change materials) and an active (thermoelectric cooler) battery thermal man-
583 agement system and their limitations, Journal of Power Sources 401 (2018) 224–237.
584 doi:10.1016/j.jpowsour.2018.08.094.

- 585 [10] R. Gulfam, P. Zhang, Z. Meng, Advanced thermal systems driven by paraffin-based
586 phase change materials – a review, *Applied Energy* 238 (2019) 582–611. doi:10.1016/
587 j.apenergy.2019.01.114.
- 588 [11] A. Arshad, H. M. Ali, M. Ali, S. Manzoor, Thermal performance of phase change
589 material (PCM) based pin-finned heat sinks for electronics devices: Effect of pin thick-
590 ness and PCM volume fraction, *Applied Thermal Engineering* 112 (2017) 143–155.
591 doi:10.1016/j.applthermaleng.2016.10.090.
- 592 [12] H. M. Ali, A. Arshad, Experimental investigation of n-eicosane based circular pin-fin
593 heat sinks for passive cooling of electronic devices, *International Journal of Heat and*
594 *Mass Transfer* 112 (2017) 649–661. doi:10.1016/j.ijheatmasstransfer.2017.05.
595 004.
- 596 [13] A. Arshad, H. M. Ali, W.-M. Yan, A. K. Hussein, M. Ahmadlouydarab, An ex-
597 perimental study of enhanced heat sinks for thermal management using n-eicosane
598 as phase change material, *Applied Thermal Engineering* 132 (2018) 52–66. doi:
599 10.1016/j.applthermaleng.2017.12.066.
- 600 [14] A. Arshad, H. M. Ali, S. Khushnood, M. Jabbal, Experimental investigation of PCM
601 based round pin-fin heat sinks for thermal management of electronics: Effect of pin-
602 fin diameter, *International Journal of Heat and Mass Transfer* 117 (2018) 861–872.
603 doi:10.1016/j.ijheatmasstransfer.2017.10.008.
- 604 [15] H. M. Ali, M. J. Ashraf, A. Giovannelli, M. Irfan, T. B. Irshad, H. M. Hamid, F. Hassan,
605 A. Arshad, Thermal management of electronics: An experimental analysis of triangular,
606 rectangular and circular pin-fin heat sinks for various PCMs, *International Journal of*
607 *Heat and Mass Transfer* 123 (2018) 272–284. doi:10.1016/j.ijheatmasstransfer.
608 2018.02.044.
- 609 [16] H. M. Ali, A. Arshad, M. M. Janjua, W. Baig, U. Sajjad, Thermal performance of LHSU
610 for electronics under steady and transient operations modes, *International Journal of*
611 *Heat and Mass Transfer* 127 (2018) 1223–1232. doi:10.1016/j.ijheatmasstransfer.
612 2018.06.120.
- 613 [17] H. M. Ali, A. Arshad, M. Jabbal, P. Verdin, Thermal management of electronics devices
614 with PCMs filled pin-fin heat sinks: A comparison, *International Journal of Heat and*

- 615 Mass Transfer 117 (2018) 1199–1204. doi:10.1016/j.ijheatmasstransfer.2017.10.
616 065.
- 617 [18] M. Al-Jethelah, S. Ebadi, K. Venkateshwar, S. Tasnim, S. Mahmud, A. Dutta, Charging
618 nanoparticle enhanced bio-based PCM in open cell metallic foams: An experimental
619 investigation, Applied Thermal Engineering 148 (2019) 1029–1042. doi:10.1016/j.
620 applthermaleng.2018.11.121.
- 621 [19] J. M. Mahdi, S. Lohrasbi, E. C. Nsofor, Hybrid heat transfer enhancement for latent-
622 heat thermal energy storage systems: A review, International Journal of Heat and Mass
623 Transfer 137 (2019) 630–649. doi:10.1016/j.ijheatmasstransfer.2019.03.111.
- 624 [20] A. Allahbakhsh, M. Arjmand, Graphene-based phase change composites for energy
625 harvesting and storage: State of the art and future prospects, Carbon 148 (2019) 441–
626 480. doi:10.1016/j.carbon.2019.04.009.
- 627 [21] J. P. Tarelho, M. P. S. dos Santos, J. A. Ferreira, A. Ramos, S. Kopyl, S. O. Kim,
628 S. Hong, A. Kholkin, Graphene-based materials and structures for energy harvesting
629 with fluids – a review, Materials Today 21 (10) (2018) 1019–1041. doi:10.1016/j.
630 mattod.2018.06.004.
- 631 [22] A. N. Keshteli, M. Sheikholeslami, Nanoparticle enhanced PCM applications for inten-
632 sification of thermal performance in building: A review, Journal of Molecular Liquids
633 274 (2019) 516–533. doi:10.1016/j.molliq.2018.10.151.
- 634 [23] A. Arshad, M. Jabbal, Y. Yan, J. Darkwa, The micro-/nano-pcms for thermal en-
635 ergy storage systems: A state of art review, International Journal of Energy Research
636 43 (11) (2019) 5572–5620. arXiv:[https://onlinelibrary.wiley.com/doi/pdf/10.](https://onlinelibrary.wiley.com/doi/pdf/10.1002/er.4550)
637 [1002/er.4550](https://onlinelibrary.wiley.com/doi/pdf/10.1002/er.4550), doi:10.1002/er.4550.
638 URL <https://onlinelibrary.wiley.com/doi/abs/10.1002/er.4550>
- 639 [24] C. Liu, Z. Rao, J. Zhao, Y. Huo, Y. Li, Review on nanoencapsulated phase change
640 materials: Preparation, characterization and heat transfer enhancement, Nano Energy
641 13 (2015) 814–826. doi:10.1016/j.nanoen.2015.02.016.
- 642 [25] F. Rodríguez-Cumplido, E. Pabón-Gelves, F. Chejne-Jana, Recent developments in the
643 synthesis of microencapsulated and nanoencapsulated phase change materials, Journal
644 of Energy Storage 24 (2019) 100821. doi:10.1016/j.est.2019.100821.

- 645 [26] E. M. Shchukina, M. Graham, Z. Zheng, D. G. Shchukin, Nanoencapsulation of phase
646 change materials for advanced thermal energy storage systems, *Chemical Society Re-*
647 *views* 47 (11) (2018) 4156–4175. doi:10.1039/c8cs00099a.
- 648 [27] M. Eugeni, H. Elahi, F. Fune, L. Lampani, F. Mastroddi, G. P. Romano, P. Gaudenzi,
649 Numerical and experimental investigation of piezoelectric energy harvester based on
650 flag-flutter, *Aerospace Science and Technology* 97 (2020) 105634. doi:10.1016/j.
651 *ast*.2019.105634.
- 652 [28] H. Elahi, M. Eugeni, P. Gaudenzi, Design and performance evaluation of a piezoelectric
653 aeroelastic energy harvester based on the limit cycle oscillation phenomenon, *Acta*
654 *Astronautica* 157 (2019) 233–240. doi:10.1016/j.actaastro.2018.12.044.
- 655 [29] A. Babapoor, G. Karimi, Thermal properties measurement and heat storage analysis of
656 paraffinnanoparticles composites phase change material: Comparison and optimization,
657 *Applied Thermal Engineering* 90 (2015) 945–951. doi:10.1016/j.applthermaleng.
658 2015.07.083.
- 659 [30] A. Babapoor, G. Karimi, S. Sabbaghi, Thermal characteristic of nanocomposite phase
660 change materials during solidification process, *Journal of Energy Storage* 7 (2016) 74–
661 81. doi:10.1016/j.est.2016.05.006.
- 662 [31] M. Nourani, N. Hamdami, J. Keramat, A. Moheb, M. Shahedi, Thermal behavior of
663 paraffin-nano-al₂O₃ stabilized by sodium stearoyl lactylate as a stable phase change
664 material with high thermal conductivity, *Renewable Energy* 88 (2016) 474–482. doi:
665 10.1016/j.renene.2015.11.043.
- 666 [32] M. Nourani, N. Hamdami, J. Keramat, A. Moheb, M. Shahedi, Preparation of a stable
667 nanocomposite phase change material (NCPCM) using sodium stearoyl lactylate (SSL)
668 as the surfactant and evaluation of its stability using image analysis, *Renewable Energy*
669 93 (2016) 404–411. doi:10.1016/j.renene.2016.02.073.
- 670 [33] M. Chieruzzi, A. Miliozzi, T. Crescenzi, L. Torre, J. M. Kenny, A new phase change
671 material based on potassium nitrate with silica and alumina nanoparticles for thermal
672 energy storage, *Nanoscale Research Letters* 10 (1). doi:10.1186/s11671-015-0984-2.
- 673 [34] R. Sharma, P. Ganesan, V. Tyagi, H. Metselaar, S. Sandaran, Thermal properties
674 and heat storage analysis of palmitic acid-TiO₂ composite as nano-enhanced organic

- 675 phase change material (NEOPCM), *Applied Thermal Engineering* 99 (2016) 1254–1262.
676 doi:10.1016/j.applthermaleng.2016.01.130.
- 677 [35] D. Yang, S. Shi, L. Xiong, H. Guo, H. Zhang, X. Chen, C. Wang, X. Chen, Paraf-
678 fin/palygorskite composite phase change materials for thermal energy storage, *Solar*
679 *Energy Materials and Solar Cells* 144 (2016) 228–234. doi:10.1016/j.solmat.2015.
680 09.002.
- 681 [36] X. Li, Y. Zhou, H. Nian, X. Zhang, O. Dong, X. Ren, J. Zeng, C. Hai, Y. Shen,
682 Advanced nanocomposite phase change material based on calcium chloride hexahydrate
683 with aluminum oxide nanoparticles for thermal energy storage, *Energy & Fuels* 31 (6)
684 (2017) 6560–6567. doi:10.1021/acs.energyfuels.7b00851.
- 685 [37] S. Sami, N. Etesami, Improving thermal characteristics and stability of phase change
686 material containing tio2 nanoparticles after thermal cycles for energy storage, *Applied*
687 *Thermal Engineering* 124 (2017) 346–352.
- 688 [38] M. Bashar, K. Siddiqui, Experimental investigation of transient melting and heat trans-
689 fer behavior of nanoparticle-enriched PCM in a rectangular enclosure, *Journal of Energy*
690 *Storage* 18 (2018) 485–497. doi:10.1016/j.est.2018.06.006.
- 691 [39] B. Praveen, S. Suresh, Experimental study on heat transfer performance of neopentyl
692 glycol/CuO composite solid-solid PCM in TES based heat sink, *Engineering Science*
693 *and Technology, an International Journal* 21 (5) (2018) 1086–1094. doi:10.1016/j.
694 *jestch.2018.07.010*.
- 695 [40] C. Li, Q. Li, L. Cong, F. jiang, Y. Zhao, C. Liu, Y. Xiong, C. Chang, Y. Ding,
696 MgO based composite phase change materials for thermal energy storage: The ef-
697 fects of MgO particle density and size on microstructural characteristics as well as
698 thermophysical and mechanical properties, *Applied Energy* 250 (2019) 81–91. doi:
699 10.1016/j.apenergy.2019.04.094.
- 700 [41] S. K. Sahoo, M. K. Das, P. Rath, Application of TCE-PCM based heat sinks for cooling
701 of electronic components: A review, *Renewable and Sustainable Energy Reviews* 59
702 (2016) 550–582. doi:10.1016/j.rser.2015.12.238.
- 703 [42] A. Arshad, M. Jabbal, Y. Yan, D. Reay, A review on graphene based nanofluids:

- 704 Preparation, characterization and applications, *Journal of Molecular Liquids* 279 (2019)
705 444–484. doi:10.1016/j.molliq.2019.01.153.
- 706 [43] A. Asadi, I. M. Alarifi, V. Ali, H. M. Nguyen, An experimental investigation on the
707 effects of ultrasonication time on stability and thermal conductivity of MWCNT-water
708 nanofluid: Finding the optimum ultrasonication time, *Ultrasonics Sonochemistry* 58
709 (2019) 104639. doi:10.1016/j.ultsonch.2019.104639.
- 710 [44] Ta instruments sdt-q600 simultaneous tga / dsc, artisan technology group, usa,
711 accessed: 01/10/2019.
712 URL [https://www.artisanTG.com/Scientific/74393-1/TA_Instruments_SDT_](https://www.artisanTG.com/Scientific/74393-1/TA_Instruments_SDT_Q600_Simultaneous_TGA_DSC)
713 [Q600_Simultaneous_TGA_DSC](https://www.artisanTG.com/Scientific/74393-1/TA_Instruments_SDT_Q600_Simultaneous_TGA_DSC)
- 714 [45] Dsc 2500, ta instruments, uk, accessed: 01/10/2019.
715 URL <https://www.tainstruments.com/dsc-2500/>
- 716 [46] Tci thermal conductivity analyzer, c-therm technologies ltd. canada, accessed:
717 01/10/2019.
718 URL https://ctherm.com/products/tci_thermal_conductivity/
- 719 [47] G. W. Burns, M. Scroger, G. Strouse, M. Croarkin, W. Guthrie, Temperature-
720 electromotive force reference functions and tables for the letter-designated thermo-
721 couple types based on the its-90, NASA STI/Recon Technical Report N 93.
- 722 [48] S. J. Kline, Describing uncertainty in single sample experiments, *Mech. Engineering* 75
723 (1953) 3–8.
- 724 [49] M. Saterlie, H. Sahin, B. Kavlicoglu, Y. Liu, O. Graeve, Particle size effects in the ther-
725 mal conductivity enhancement of copper-based nanofluids, *Nanoscale Research Letters*
726 6 (1) (2011) 217. doi:10.1186/1556-276x-6-217.
- 727 [50] W. Evans, R. Prasher, J. Fish, P. Meakin, P. Phelan, P. Keblinski, Effect of aggrega-
728 tion and interfacial thermal resistance on thermal conductivity of nanocomposites and
729 colloidal nanofluids, *International Journal of Heat and Mass Transfer* 51 (5-6) (2008)
730 1431–1438. doi:10.1016/j.ijheatmasstransfer.2007.10.017.
- 731 [51] F. Bakhtiari, E. Darezereshki, One-step synthesis of tenorite (CuO) nano-particles from

- 732 cu4 (SO4) (OH) 6 by direct thermal-decomposition method, *Materials Letters* 65 (2)
733 (2011) 171–174. doi:10.1016/j.matlet.2010.09.071.
- 734 [52] M. Faisal, S. B. Khan, M. M. Rahman, A. Jamal, A. Umar, Ethanol chemi-sensor:
735 Evaluation of structural, optical and sensing properties of CuO nanosheets, *Materials*
736 *Letters* 65 (9) (2011) 1400–1403. doi:10.1016/j.matlet.2011.02.013.
- 737 [53] Y. Chen, W. Luo, J. Wang, J. Huang, Enhanced thermal conductivity and durability
738 of a paraffin wax nanocomposite based on carbon-coated aluminum nanoparticles, *The*
739 *Journal of Physical Chemistry C* 121 (23) (2017) 12603–12609. doi:10.1021/acs.
740 jpc.7b02651.
- 741 [54] F. Yavari, H. R. Fard, K. Pashayi, M. A. Rafiee, A. Zamiri, Z. Yu, R. Ozisik, T. Borca-
742 Tasciuc, N. Koratkar, Enhanced thermal conductivity in a nanostructured phase change
743 composite due to low concentration graphene additives, *The Journal of Physical Chem-*
744 *istry C* 115 (17) (2011) 8753–8758. doi:10.1021/jp200838s.
- 745 [55] H. Liu, X. Wang, D. Wu, Fabrication of graphene/TiO₂/paraffin composite phase
746 change materials for enhancement of solar energy efficiency in photocatalysis and la-
747 tent heat storage, *ACS Sustainable Chemistry & Engineering* 5 (6) (2017) 4906–4915.
748 doi:10.1021/acssuschemeng.7b00321.
- 749 [56] H. Tian, W. Wang, J. Ding, X. Wei, M. Song, J. Yang, Thermal conductivities and
750 characteristics of ternary eutectic chloride/expanded graphite thermal energy storage
751 composites, *Applied Energy* 148 (2015) 87–92. doi:10.1016/j.apenergy.2015.03.
752 020.
- 753 [57] J. Wang, H. Xie, Z. Xin, Y. Li, L. Chen, Enhancing thermal conductivity of palmitic
754 acid based phase change materials with carbon nanotubes as fillers, *Solar Energy* 84 (2)
755 (2010) 339–344. doi:10.1016/j.solener.2009.12.004.
- 756 [58] O. Mahian, L. Kolsi, M. Amani, P. Estellé, G. Ahmadi, C. Kleinstreuer, J. S. Mar-
757 shall, M. Siavashi, R. A. Taylor, H. Niazmand, S. Wongwises, T. Hayat, A. Kolan-
758 jiyil, A. Kasaeian, I. Pop, Recent advances in modeling and simulation of nanofluid
759 flows-part i: Fundamentals and theory, *Physics Reports* 790 (2019) 1–48. doi:
760 10.1016/j.physrep.2018.11.004.

- 761 [59] M. Mehrali, S. T. Latibari, M. Mehrali, T. M. I. Mahlia, E. Sadeghinezhad, H. S. C.
762 Metselaar, Preparation of nitrogen-doped graphene/palmitic acid shape stabilized com-
763 posite phase change material with remarkable thermal properties for thermal energy
764 storage, *Applied Energy* 135 (2014) 339–349. doi:10.1016/j.apenergy.2014.08.100.
- 765 [60] A. A. Aydın, A. Aydın, High-chain fatty acid esters of 1-hexadecanol for low tempera-
766 ture thermal energy storage with phase change materials, *Solar Energy Materials and*
767 *Solar Cells* 96 (2012) 93–100. doi:10.1016/j.solmat.2011.09.013.
- 768 [61] E. Hellstern, H. J. Fecht, Z. Fu, W. L. Johnson, Structural and thermodynamic prop-
769 erties of heavily mechanically deformed ru and AlRu, *Journal of Applied Physics* 65 (1)
770 (1989) 305–310. doi:10.1063/1.342541.
- 771 [62] B.-X. Wang, L.-P. Zhou, X.-F. Peng, Surface and size effects on the specific heat ca-
772 pacity of nanoparticles, *International Journal of Thermophysics* 27 (1) (2006) 139–151.
773 doi:10.1007/s10765-006-0022-9.
- 774 [63] L. Wang, Z. Tan, S. Meng, D. Liang, G. Li, Enhancement of molar heat capacity
775 of nanostructured al₂o₃, *Journal of Nanoparticle Research* 3 (5/6) (2001) 483–487.
776 doi:10.1023/a:1012514216429.
- 777 [64] E. V. Timofeeva, J. L. Routbort, D. Singh, Particle shape effects on thermophysical
778 properties of alumina nanofluids, *Journal of Applied Physics* 106 (1) (2009) 014304.
779 doi:10.1063/1.3155999.
- 780 [65] H. Xie, J. Wang, T. Xi, Y. Liu, F. Ai, Q. Wu, Thermal conductivity enhancement of
781 suspensions containing nanosized alumina particles, *Journal of Applied Physics* 91 (7)
782 (2002) 4568–4572. doi:10.1063/1.1454184.
- 783 [66] H. D. Koca, S. Doganay, A. Turgut, I. H. Tavman, R. Saidur, I. M. Mahbubul, Effect
784 of particle size on the viscosity of nanofluids: A review, *Renewable and Sustainable*
785 *Energy Reviews* 82 (2018) 1664–1674. doi:10.1016/j.rser.2017.07.016.
- 786 [67] Z. Le-Ping, W. Bu-Xuan, P. Xiao-Feng, X.-Z. Du, Y. Yong-Ping, On the specific heat
787 capacity of cuo nanofluid, *Advances in Mechanical Engineering* 02 (2010) 1–4. doi:
788 10.1155/2010/172085.